Astronomy & Astrophysics manuscript no. output
May 5, 2026

The influence of the fractal dimension on dust evolution in protoplanetary disks

J. E. Schöll[1], C. P. Dullemond[1], and C. Dominik[2]

[1] Institut für Theoretische Astrophysik, Zentrum für Astronomie der Universität Heidelberg, Albert-Ueberle-Str. 2, 69120 Heidelberg, Germany
[2] Anton Pannekoek Institute for Astronomy, University of Amsterdam, Science Park 904, 1098 XH Amsterdam, The Netherlands

Received September 30, 20XX

ABSTRACT

Context. During the first stages of dust coagulation in protoplanetary disks, the dust aggregates are expected to have a high degree of porosity. Most models of dust growth, however, do not take this into account. The reason for this is the technical complexity of this problem. Furthermore, the coagulation kernel for colliding porous or fractal dust aggregates is not well understood.
Aims. We wish to explore the effect of aggregate porosity on the evolution of the dust population in protoplanetary disks, with an emphasis on the fragmentation and the bouncing barrier.
Methods. We use the DustPy code, and implement porosity as a prescribed function of particle mass with the fractal dimension as a free parameter. In this way, we parameterize the ill-constrained physics of colliding porous or fractal aggregates, and we can explore the effect of different porosity prescriptions. We take into account the effect of porosity on the dust dynamics, while neglecting its effect on the collision outcomes.
Results. We find that larger particle masses are reached for lower fractal dimensions. The maximum Stokes numbers that are reached do not depend on the fractal dimension in the case of fragmentation-limited growth and decrease with decreasing fractal dimension in the case of bouncing-limited growth. Furthermore, particle growth is slower for smaller fractal dimensions in our models.
Conclusions. Dust evolution is strongly influenced by the fractal dimension. Although larger masses are reached for smaller fractal dimensions, the particles are still much smaller than planetesimals. Under the assumption that the bouncing and fragmentation velocities do not depend on the fractal dimension or filling factor, fractal growth is not beneficial for the streaming instability to occur in the case of fragmentation-limited growth and even disadvantageous in the case of bouncing-limited growth.

Key words. methods: numerical – planet and satellites: formation – protoplanetary disks

1. Introduction

The coagulation of dust in protoplanetary disks is the first step on the path to the formation of planets and planetary systems. It has been studied extensively for decades, but progress is slow because realistic simulations require enormous resources, laboratory measurements are scarce, and observational constraints are only very indirect. As a result, the process of dust growth is still not sufficiently well understood.

What we do know is that the collisional growth of dust aggregates encounters several so-called growth barriers, such as the drift barrier (e.g., Weidenschilling 1977; Brauer et al. 2008); the bouncing barrier (e.g., Blum & Wurm 2008; Zsom et al. 2010; Dominik & Dullemond 2024); the fragmentation barrier (e.g., Birnstiel et al. 2012); and the electrostatic barrier (e.g., Okuzumi 2009). To produce larger bodies, mechanisms such as the streaming instability (Youdin & Goodman 2005; Johansen & Youdin 2007; Johansen et al. 2007) are necessary. For the streaming instability to set in, the dust aggregates must grow to some minimal size, or more precisely to a minimal Stokes number. Planetesimal formation is thus a two-stage process: first growth of dust aggregates to pebble size, which are then collected into planetesimals by the streaming instability. Where and when grain growth manages to reach the right conditions for this to occur depends on the details of the grain growth process, which are hard to model.

In this paper we study how dust aggregate porosity, expressed in terms of a fractal growth model, affects the evolution of the dust distribution in a protoplanetary disk. To explain the challenges of this problem and our method for addressing them, we first briefly review the algorithms used in modern dust evolution models.

The computational modeling of grain growth falls into one of two classes. One class of models simulates individual collisions of two dust aggregates, each consisting of a multitude of monomers, and follows its outcome (e.g., Dominik & Tielens 1997; Suyama et al. 2008; Wada et al. 2007, 2008, 2009, 2011). These models determine whether the collision leads to sticking, bouncing, or fragmentation and how the structure of the aggregates changes in the collision. These are the most detailed dust coagulation models and can be compared directly with laboratory experiments (e.g., Schräpler et al. 2012). The other class of models simulates the evolution of a population of dust particles. While numerous approximate methods have been proposed (e.g., Estrada & Cuzzi 2008; Birnstiel et al. 2012), two popular classes of models attempt to compute the evolution of the full grain size distribution: the Monte Carlo approach (e.g., Ormel et al. 2007; Zsom & Dullemond 2008; Beutel & Dullemond 2023), and the Smoluchowski equation approach (Weidenschilling 1997; Tanaka et al. 2005; Dullemond & Dominik 2005).

In the Monte Carlo method, the very large number of true particles ($\sim 10^{30}$ or more, for particles of μm size) is repre-

Article published by EDP Sciences, to be cited as https://doi.org/10.1051/0004-6361/202558375

sented by a computationally feasible number of computational particles. The advantage of this approach is that each computational particle can easily be assigned an arbitrary number of auxiliary properties (e.g., porosity, charge, composition). The Monte Carlo method has been used to study the effect of porosity on the size distribution (e.g., Ormel et al. 2007; Zsom et al. 2010; Krijt et al. 2015; Lorek et al. 2018; Xiang et al. 2020), demonstrating its importance.

In the approach using the Smoluchowski equation (Smoluchowski 1916), the particle size distribution is computed directly in the form $N(m,t)$, where $N(m,t)\mathrm{d}m$ is the number of particles with masses between m and $m+\mathrm{d}m$ at time t. To do so, the mass coordinate is divided into ∼100 logarithmically-spaced bins between the smallest and the largest dust aggregate mass. The advantage of this method is the higher dynamic range in mass and the possibility to use implicit integration schemes to evolve the distribution over long timescales. For global disk models, the Smoluchowski approach is typically more efficient than the Monte Carlo approach. However, the disadvantage is that any additional independent property, such as the volume filling factor ϕ, adds another dimension, which is often computationally too expensive. A solution to this problem would be to introduce the volume filling factor ϕ as a dependent variable $\phi(m,t)$. Models of this type (Okuzumi et al. 2012; Estrada et al. 2022; Michoulier et al. 2024) remain efficient, while still being able to treat porosity in some detail. This requires a treatment of how porosity changes with time in the coagulation process, and as a result of, for instance, gas drag or self-gravity.

In the present paper, we choose to take a slightly simpler approach, in which we prescribe $\phi(m)$ beforehand, so that we do not need to compute it on the fly. The advantage of this simplification is that we can explore the effects of, for instance, a fractal dimension, without settling on a detailed model of how porosity is changing as a function of the evolving dust distribution. Our result will thus have wider validity, at the cost of a reduced predictivity and falsifiability. We base our prescription on the work of Okuzumi et al. (2012), Krijt et al. (2015), Estrada et al. (2022), and Tazaki (2021). Our goal is to improve the understanding of the effect and importance of including porosity in computations of the dust evolution in global models of protoplanetary disks, especially in light of the importance of the fragmentation barrier and the bouncing barrier.

The paper is structured as follows. In Sect. 2, we describe the general model setup. In Sect. 3, we apply a prescription for fractal growth using simple expressions for the cross sections and present the results of these models. Thereafter, we present models with more elaborate expressions for the cross sections in Sect. 4. Then, we discuss some aspects of our results in Sect. 5 and summarize our conclusions in Sect. 6.

2. General model setup

We used the Python tool `DustPy` v.1.0.6 (Stammler & Birnstiel 2022) to model the dust evolution. `DustPy` applies a 1D disk model and solves the advection-diffusion equation for gas and dust transport in the radial direction, as well as the Smoluchowski equation for dust growth.

2.1. Disk model

Our disk ranges from $r_{\rm in} = 1$ au to $r_{\rm out} = 10^3$ au, with 100 logarithmically spaced grid cells. The central star has a mass of $M_\star = 1M_\odot$, a radius of $R_\star = 2R_\odot$, and a temperature of $T_\star = 5772$ K.

For the initial gas surface density, we apply the self-similar solution of Lynden-Bell & Pringle (1974), which is given by

$$\Sigma_{\rm g}(r) = \frac{M_{\rm gas}}{2\pi r_{\rm c}^2}\left(\frac{r}{r_{\rm c}}\right)^{-1}\exp\left(-\frac{r}{r_{\rm c}}\right), \tag{1}$$

where we chose the cut-off radius $r_{\rm c} = 60$ au and the gas mass of $M_{\rm gas} = 10^{-2}M_\odot$.

For the temperature, it is assumed that the disk is passively irradiated at a constant irradiation angle of 0.05 rad, which yields

$$T(r) = T_\star\left(\frac{0.05}{2}\right)^{1/4}\left(\frac{r}{R_\star}\right)^{-1/2}. \tag{2}$$

In the vertical direction to the disk midplane, isothermal hydrostatic equilibrium is assumed (Stammler & Birnstiel 2022). The mean mass of the gas particles is $\overline{m} = 2.3m_{\rm p}$, where $m_{\rm p}$ is the proton mass.

2.2. Dust model

The mass grid is logarithmic, with seven bins per decade. The grid ranges from $m_{\rm min} = 10^{-12}$ g to $m_{\rm max} = 10^5$ g when bouncing is active and from $m_{\rm min} = 10^{-12}$ g to $m_{\rm max} = 10^8$ g when bouncing is inactive.

Initially, the dust-to-gas-ratio $\Sigma_{\rm d}/\Sigma_{\rm g}$ is set to 0.01. For the initial size distribution, we adopted the Mathis-Rumple-Nordsieck (MRN) distribution $n(a) \propto a^{-7/2}$ (Mathis et al. 1977), up to a maximum size of $a_{\rm ini,max} = 10^{-4}$ cm. In the outer part of the disk, even such small grains can have drift timescales smaller than their growth timescales. These grains are removed from the initial dust distribution (for details, see `DustPy` documentation[1]).

We assumed a material density of $\rho_{\rm s} = 1.67$ g cm^{-3}. Dust aggregates are a collection of small dust grains, so-called monomers. For a standard `DustPy` simulation, it is not necessary to determine the monomer size. However, since we included bouncing and fractal growth, we needed to determine the monomer size, which we set to $a_\bullet = 10^{-4}$ cm. Although monomer grains are likely of irregular shape in reality (Güttler et al. 2019), we assumed them to be compact spheres for simplicity.

The vertical dust density profile is assumed to be Gaussian with the dust scale height (Dubrulle et al. 1995)

$$h = H_{\rm P}\sqrt{\frac{\alpha}{\alpha+{\rm St}}}, \tag{3}$$

where $H_{\rm P}$ is the pressure scale height of the gas, α is the turbulent viscosity parameter introduced by Shakura & Sunyaev (1973), and St is the Stokes number, which is a measure of the coupling between dust and gas. It is given by (Stammler & Birnstiel 2022)

$${\rm St} = \begin{cases} \dfrac{\pi}{2}\dfrac{a\rho}{\Sigma_{\rm g}} & \text{for } a < \frac{9}{4}\lambda_{\rm mfp} \text{ (Epstein regime)},\\ \dfrac{2\pi}{9}\dfrac{a^2\rho}{\lambda_{\rm mfp}\Sigma_{\rm g}} & \text{else (Stokes regime)}, \end{cases} \tag{4}$$

where a is the size of the particle, ρ is the bulk density of the particle, and $\lambda_{\rm mfp}$ is the mean free path of the gas.

[1] https://stammler.github.io/dustpy/

2.3. Relative velocities

DustPy considers Brownian motion, radial and azimuthal drift, vertical settling, and turbulence as sources for relative velocities between dust particles. For turbulent relative velocities, the model of Ormel & Cuzzi (2007) is applied, which considers different turbulence regimes. The turbulent relative velocities increase steeply, when the stopping time $t_s = \mathrm{St}/\Omega_K$ of the larger particle exceeds the Kolmogorov time $t_\eta = \Omega_K^{-1}\mathrm{Re}^{-1/2}$, which corresponds to the eddy turnover time of the smallest turbulent eddies. $\mathrm{Re} = \nu_t/\nu_{mol}$ is the Reynolds number, which is defined as the ratio between turbulent viscosity $\nu_t = \alpha c_s H_P$ and molecular viscosity $\nu_{mol} = \sqrt{8/\pi} c_s \lambda_{mfp}/2$, where c_s is the sound speed[2].

Contributions of turbulence (for $t_s < t_\eta$), radial drift, azimuthal drift, and vertical settling to relative velocities depend on the difference between the Stokes numbers of the collision partners. Therefore, for two particles with the same Stokes number, the only contribution to relative velocities is Brownian motion. This is particularly relevant for a fractal dimension of $D = 2$, because in this case the Stokes number, which is proportional to the mass-to-area ratio m/A_{aero}, does not depend on the mass if the aerodynamical cross sections are given by $A_{aero} = \pi a^2$. If more elaborate expressions are applied for cross sections, m/A_{aero} approaches a constant value for large N if $D \lesssim 2$ (e.g., Ormel et al. 2007; Okuzumi et al. 2011). However, as pointed out by Okuzumi et al. (2011), the dispersion of the cross-sectional area (referred to as area dispersion from now on) cannot be neglected in this case, meaning that two particles of the same mass can have slightly different cross sections due to statistical variations.

We assumed that Stokes numbers follow a narrow log-normal distribution for each particle's mass. We then averaged over the relative velocity equations and expressed them in terms of the mean Stokes numbers of the respective masses. This led to the appearance of additional terms, which are nonzero, even if the mean Stokes numbers are the same. The detailed derivation and the resulting expressions are shown in Appendix A.1.

The width of the dispersion is parametrized by the parameter ϵ. Okuzumi et al. (2011) measured the value of ϵ in their numerical models of fractal aggregates and found $\epsilon \approx 0.1$, which we adopted. To verify its importance, we also ran models without area dispersion, which are shown in Appendix A.2.

2.4. Collision model

By default, DustPy has two possible collision outcomes: sticking and fragmentation. If the relative velocity v_{rel} between two collision partners is below a threshold velocity v_f, then the collision results in perfect sticking. Otherwise, the collision results in fragmentation. DustPy further differentiates between full fragmentation for aggregates of similar size and erosion, if the mass ratio of the collision partners exceeds a critical mass ratio r_m, which we set to $r_m = 10$. In a full fragmentation event, the fragment mass is the total mass of both collision partners; in an erosion event, the larger particle only loses a part of its mass, which we chose to be equal to the mass of the smaller particle. The fragment distribution is $f(m)\mathrm{d}m \propto m^{-11/6}\mathrm{d}m$, which again corresponds to the MRN distribution.

In DustPy, the relative velocities are assumed to follow a Maxwell-Boltzmann distribution, where the single velocity computed for each pair of masses at each radial location corresponds to the root-mean-square velocity of the Maxwell-Boltzmann distribution. Thus, even if the root-mean-square velocity is higher than the fragmentation velocity v_f, there is a chance that the collision partners have a lower velocity and the collision does not result in fragmentation. For details, see Stammler & Birnstiel (2022).

Dominik & Dullemond (2024) extend the collision model to also take into account bouncing. They define the bouncing velocity as

$$v_b(m_1, m_2) = \min\left[v_s(m_1, m_2), v_f\right], \tag{5}$$

where m_1 and m_2 are the masses of the collision partners, respectively, and v_s is the sticking velocity, which is given by (Dominik & Tielens 1997; Güttler et al. 2010)

$$v_s(m_1, m_2) = \sqrt{5\pi a_\bullet F_{roll} \frac{m_1 + m_2}{m_1 m_2}}, \tag{6}$$

with rolling force F_{roll}. It is defined as the force that is necessary to roll a monomer over another monomer. Collisions with relative velocities between v_b and v_f result in bouncing, i.e., the masses of both collision partners stay the same. For details on the implementation of bouncing in DustPy, see Dominik & Dullemond (2024).

Studies suggest that the filling factor also affects collision outcomes (e.g., Güttler et al. 2010; Wada et al. 2011; Gunkelmann et al. 2016; Arakawa et al. 2023; Oshiro et al. 2025). However, there is still much uncertainty when it comes to the influence of the filling factor on collision outcomes.

To keep things simple, we did not consider the effect of the filling factor on the collision outcome, but we investigated models with bouncing and models without bouncing. The limitations of our simple collision model are discussed in Sect. 5.1. Following Dominik & Dullemond (2024), we set the fragmentation velocity at $v_f = 100$ cm s^{-1} and the rolling force at $F_{roll} = 10^{-4}$ dyn.

3. Fractal model

In this work, we did not model fractal growth by evolving the volume-filling factor numerically. Instead, we modeled fractal growth using a fixed prescription for the filling factor as a function of mass and treated the fractal dimension as a free parameter. This allowed us to investigate different degrees of fractality, i.e., different fractal dimensions.

In this section we treat the cross sections of fractal particles in a simplified way by approximating them with the cross sections of spherical particles (for details, see Sect. 3.1). This allows us to easily adjust existing estimates for the growth barriers to the case of fractal growth (Sect. 3.2 and Appendix C), which helps us to better understand the numerical results. In Sect. 4, we apply a more elaborate, semi-analytic expression for the cross sections of fractal particles, and compare the results to those of the models with the simple expression.

3.1. Porosity model

The filling factor ϕ of a dust aggregate is defined as the volume fraction that is filled with material. Hence, it can be written as the ratio $\phi = \rho/\rho_s$ between the bulk density ρ of the aggregate and the material density ρ_s of the monomer grains (e.g., Kataoka et al. 2013b).

In the first phase of dust coagulation, the impact energies are too small to lead to significant compaction of the aggregates.

[2] DustPy v.1.0.6 uses the adiabatic sound speed to compute turbulent relative velocities, with an adiabatic coefficient of $\gamma = 1.4$. In newer versions of DustPy, the isothermal sound speed is used, which is more appropriate. However, the deviation is only small (a factor of $\sqrt{\gamma}$).

Therefore, the particles become more and more porous as they grow (Dominik & Tielens 1997), and the filling factor decreases. This can be described by the fractal dimension D, which is defined by the relation

$$m \propto a^D. \tag{7}$$

The fractal dimension is $D = 3$ for nonfractal growth and $D < 3$ for fractal growth.

The definition of the radius of a fractal particle is ambiguous. Often, the radius of gyration is used (e.g., Wada et al. 2007, 2008; Okuzumi et al. 2009), which is given by

$$a_\mathrm{g} = \sqrt{\frac{1}{N}\sum_{k=1}^{N}(\mathbf{x}_k - \mathbf{x}_\mathrm{s})^2}, \tag{8}$$

where N is the number of monomers, $\mathbf{x}_k$ ($k = 1, 2, ..., N$) are their positions, and $\mathbf{x}_\mathrm{s}$ is the center of mass. The gyration radius follows the relation (Tazaki 2021)

$$a_\mathrm{g} = a_\bullet \left(\frac{m}{k_0 m_\bullet}\right)^{1/D}, \tag{9}$$

where $m_\bullet$ is the monomer mass and k_0 is the fractal pre-factor, which depends on the fractal dimension. Equation (9) does not hold for small m if $k_0 \neq 1$, since it does not recover the monomer radius for $m = m_\bullet$.

For the simple prescription of the filling factor in this section, we omit the fractal pre-factor in Eq. (9) and define the particle radius in terms of mass and fractal dimension as

$$a = a_\bullet \left(\frac{m}{m_\bullet}\right)^{1/D}. \tag{10}$$

At some point, the collision energies become large enough to lead to the restructuring and compaction of the aggregates (Dominik & Tielens 1997; Güttler et al. 2010).

Michoulier et al. (2024) modeled the evolution of porosity and included collisional compaction. In their models, fractal growth proceeds also after collisional compaction sets in, but with a larger fractal dimension than before. Other studies find that fractal growth terminates once collision energies become large enough to lead to compaction. The filling factor then stays approximately constant (Okuzumi et al. 2012; Krijt et al. 2015; Estrada et al. 2022).

We accounted for this by introducing a minimum filling factor ϕ_min. When particles reach this minimum filling factor, growth proceeds nonfractally and the filling factor stays constant. In reality, the minimum filling factor is a function of the radial distance (Okuzumi et al. 2012) but for simplicity, we assumed that it would be constant throughout the disk. Furthermore, very large aggregates can also be compressed by gas ram pressure and self-gravity (Kataoka et al. 2013a; Estrada et al. 2022; Michoulier et al. 2024). Since the focus of this work is on the influence of the fractal dimension, we did not consider compaction by gas ram pressure and self-gravity.

The mass domain extends to smaller masses than the monomer mass. For masses $m < m_\bullet$, we assumed $\phi = 1$. Therefore, the full expression for the particle radius as a function of mass is given by

$$a(m) = \begin{cases} a_\bullet \left(\dfrac{m}{m_\bullet}\right)^{1/3} & \text{for } m < m_\bullet, \\ a_\bullet \left(\dfrac{m}{m_\bullet}\right)^{1/D} & \text{for } m_\bullet \leq m \leq m_\bullet \phi_\mathrm{min}^{D/(D-3)}, \\ a_\bullet \phi_\mathrm{min}^{-1/3} \left(\dfrac{m}{m_\bullet}\right)^{1/3} & \text{for } m_\bullet \phi_\mathrm{min}^{D/(D-3)} < m, \end{cases} \tag{11}$$

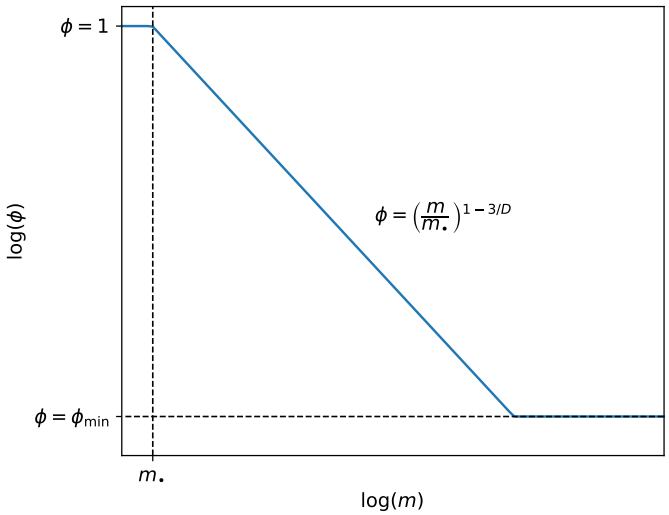

Fig. 1: Filling factor ϕ as a function of mass for the SC models.

and the full expression for the filling factor is given by

$$\phi(m) = \begin{cases} 1 & \text{for } m < m_\bullet, \\ \max\left[\left(\dfrac{m}{m_\bullet}\right)^{1-3/D}, \phi_\mathrm{min}\right] & \text{else.} \end{cases} \tag{12}$$

The collision cross section between particles is given by

$$A_\mathrm{coll} = \pi (a_1 + a_2)^2, \tag{13}$$

where a_1 and a_2 are the radii of the collision partners, respectively. For the aerodynamical cross section, we applied the expression

$$A_\mathrm{aero} = \pi a^2, \tag{14}$$

which corresponds to the cross section of a sphere of radius a. This is of course a simplification, because in reality fractal particles are not spherical and their cross sections take a more complicated form. We therefore also investigated models with more elaborate cross sections, which are presented in Sect. 4.

Using the expression of Eq. (14) has the consequence that the fractal dimension can only take values between $2 \leq D \leq 3$. Values $D < 2$ would imply that the aerodynamical cross section of an aggregate is larger than the sum of the aerodynamical cross sections of all its monomers, which is unphysical. We will refer to the models that apply the above porosity prescription as simple cross-sectional (SC) models. Figure 1 shows the filling factor as a function of mass for the SC models as given by Eq. (12). The mass-radius relations of the SC models are shown in Fig. 2.

3.2. Growth barriers

The dust distribution is shaped by several growth barriers. The drift barrier is related to the fact that in some Stokes numbers, particles drift inward rapidly enough to get lost in the evaporation zone before they can grow to larger sizes (e.g., Weidenschilling 1977; Brauer et al. 2008). The fragmentation barrier (e.g., Birnstiel et al. 2012) and the bouncing barrier (e.g., Blum & Wurm 2008; Zsom et al. 2010; Dominik & Dullemond 2024) are related to the fact that collisions result in bouncing or fragmentation, once the collision energies exceed the corresponding threshold (see Sect. 2.4).

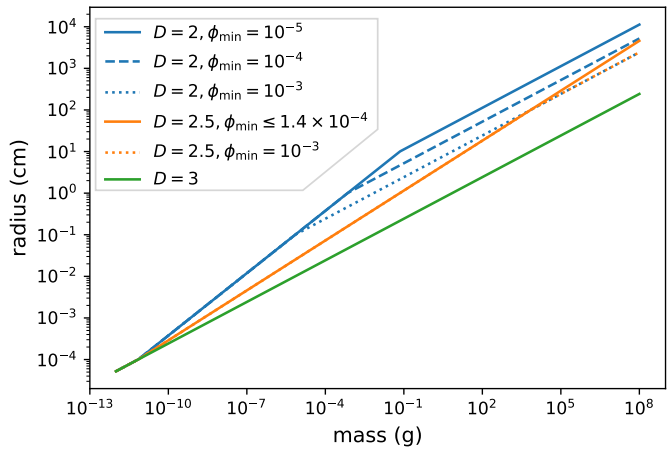

Fig. 2: Mass-radius relation for the SC models.

Table 1: Properties of the SC models.

	Model name	D	$\phi_{\min}$	α	bo.?
Vary D	SC_D3_a4	3	-	10^{-4}	yes
	SC_D25_fm5_a4	2.5	10^{-5}	10^{-4}	yes
	SC_D2_fm5_a4	2	10^{-5}	10^{-4}	yes
	SC_D3_a4_nobo	3	-	10^{-4}	no
	SC_D25_fm5_a4_nobo	2.5	10^{-5}	10^{-4}	no
	SC_D2_fm5_a4_nobo	2	10^{-5}	10^{-4}	no
Vary $\phi_{\min}$	SC_D2_fm3_a4	2	10^{-3}	10^{-4}	yes
	SC_D2_fm4_a4	2	10^{-4}	10^{-4}	yes
	SC_D2_fm3_a4_nobo	2	10^{-3}	10^{-4}	no
	SC_D2_fm4_a4_nobo	2	10^{-4}	10^{-4}	no
Vary α	SC_D3_a6	3	-	10^{-6}	yes
	SC_D3_a3	3	-	10^{-3}	yes
	SC_D25_fm5_a6	2.5	10^{-5}	10^{-6}	yes
	SC_D25_fm5_a3	2.5	10^{-5}	10^{-3}	yes
	SC_D2_fm5_a6	2	10^{-5}	10^{-6}	yes
	SC_D2_fm5_a3	2	10^{-5}	10^{-3}	yes
	SC_D3_a6_nobo	3	-	10^{-6}	no
	SC_D3_a3_nobo	3	-	10^{-3}	no
	SC_D25_fm5_a6_nobo	2.5	10^{-5}	10^{-6}	no
	SC_D25_fm5_a3_nobo	2.5	10^{-5}	10^{-3}	no
	SC_D2_fm5_a6_nobo	2	10^{-5}	10^{-6}	no
	SC_D2_fm5_a3_nobo	2	10^{-5}	10^{-3}	no

Notes. The last column shows whether bouncing is included or not. The SC in the model name stands for the simple cross sections. The number following D stands for the fractal dimension, where the decimal point is omitted. The number following fm is the negative logarithm of ϕ. The number following a is the negative logarithm of α. If the name ends with nobo, the model does not include bouncing.

Following Birnstiel et al. (2012), we compare the drift timescale $\tau_{\rm drift} = r/|v_{\rm d}|$, where r is the radial distance to the central star and $v_{\rm d}$ is the drift velocity, to the growth timescale $\tau_{\rm grow} = a/\dot{a}$, where $\dot{a}$ is the change of size per unit time of the particle. This yields the maximum Stokes number that the grains can reach before drifting inward faster than growing further (Birnstiel et al. 2012)

$$\mathrm{St_d} = \frac{\Sigma_{\rm d}}{\Sigma_{\rm g}} \frac{v_{\rm K}^2}{c_{\rm s}^2} \left| \frac{\mathrm{d} \ln P}{\mathrm{d} \ln r} \right|^{-1}, \tag{15}$$

where P is the gas pressure and $v_{\rm K} = r\Omega_{\rm K}$ is the Kepler velocity, with the Kepler frequency $\Omega_{\rm K}$. Equation (15) shows that $\mathrm{St_d}$ does not depend on particle properties.

The Stokes number corresponding to the fragmentation barrier can be derived by comparing the relative velocities to the fragmentation velocity and is given by (Birnstiel et al. 2009)

$$\mathrm{St_f} = \frac{1}{3} \frac{v_{\rm f}^2}{\alpha c_{\rm s}^2}, \tag{16}$$

where it is assumed that turbulence dominates the relative velocities and $v_{\rm rel} \approx 3\sqrt{\alpha \mathrm{St}} c_{\rm s}$. The Stokes number corresponding to the bouncing barrier is given by (Dominik & Dullemond 2024)

$$\mathrm{St_b} = \max\left[\frac{1}{3} \frac{v_{\rm b}^2}{\alpha c_{\rm s}^2}, \mathrm{St}_\eta \right], \tag{17}$$

where $\mathrm{St}_\eta = \mathrm{Re}^{-1/2}$ is the Stokes number, at which the particles' stopping time $t_{\rm s}$ exceeds the Kolmogorov time t_η. We introduced it following Dominik & Dullemond (2024) to account for the fact that the contribution of turbulence to the relative velocities is much smaller for $t_{\rm s} < t_\eta$ than for $t_{\rm s} > t_\eta$. In contrast to $v_{\rm f}$, the bouncing velocity is a function of mass. Thus, while $\mathrm{St_f}$ does not depend on particle properties (except for the value of $v_{\rm f}$), $\mathrm{St_b}$ is not independent of particle properties, since the relation between St and mass depends on properties such as the fractal dimension or the filling factor.

Equations (15), (16), and (17) can be solved for the mass to yield the respective growth barriers in terms of mass. This is shown in Appendix C. The estimates predict that the dust distribution of models with smaller fractal dimensions reach larger masses due to their smaller Stokes numbers, which lead to smaller relative velocities.

The smallest particles in a bouncing-limited dust distribution collide mainly with larger particles. The minimum energy required for collisions to result in bouncing is set by the adopted bouncing threshold velocity (see Eqs. (5) and (6)). From Eq. (6), it can be deduced that the collision energy involved in collisions with larger particles is typically larger than that involved in collisions with equal-sized or smaller particles. Therefore, the smallest particles of the mass distribution reach the bouncing barrier already at smaller masses. We exploit this fact to derive an estimate of the lower edge of the mass distribution, which we will refer to as the "lower bouncing barrier", as opposed to the usual bouncing barrier, which corresponds to the upper edge of the mass distribution. We derive the lower bouncing barrier in Appendix C.

3.3. Influence of the fractal dimension

To investigate the influence of fractal dimensions on dust evolution, we ran models with highly fractal ($D = 2$), moderately fractal ($D = 2.5$), and nonfractal ($D = 3$) growth. For these fiducial models, we chose $\phi_{\min} = 10^{-5}$, roughly corresponding to the value found by previous studies (Okuzumi et al. 2012; Krijt et al. 2015; Estrada et al. 2022) and $\alpha = 10^{-4}$, but also investigated different minimum filling factors (Sect. 3.4) and turbulent viscosity parameters (Sect. 3.5). For each fractal dimension, we ran a model with bouncing and one without bouncing. The properties of the models are shown in Table 1. The models were run for 10^6 years.

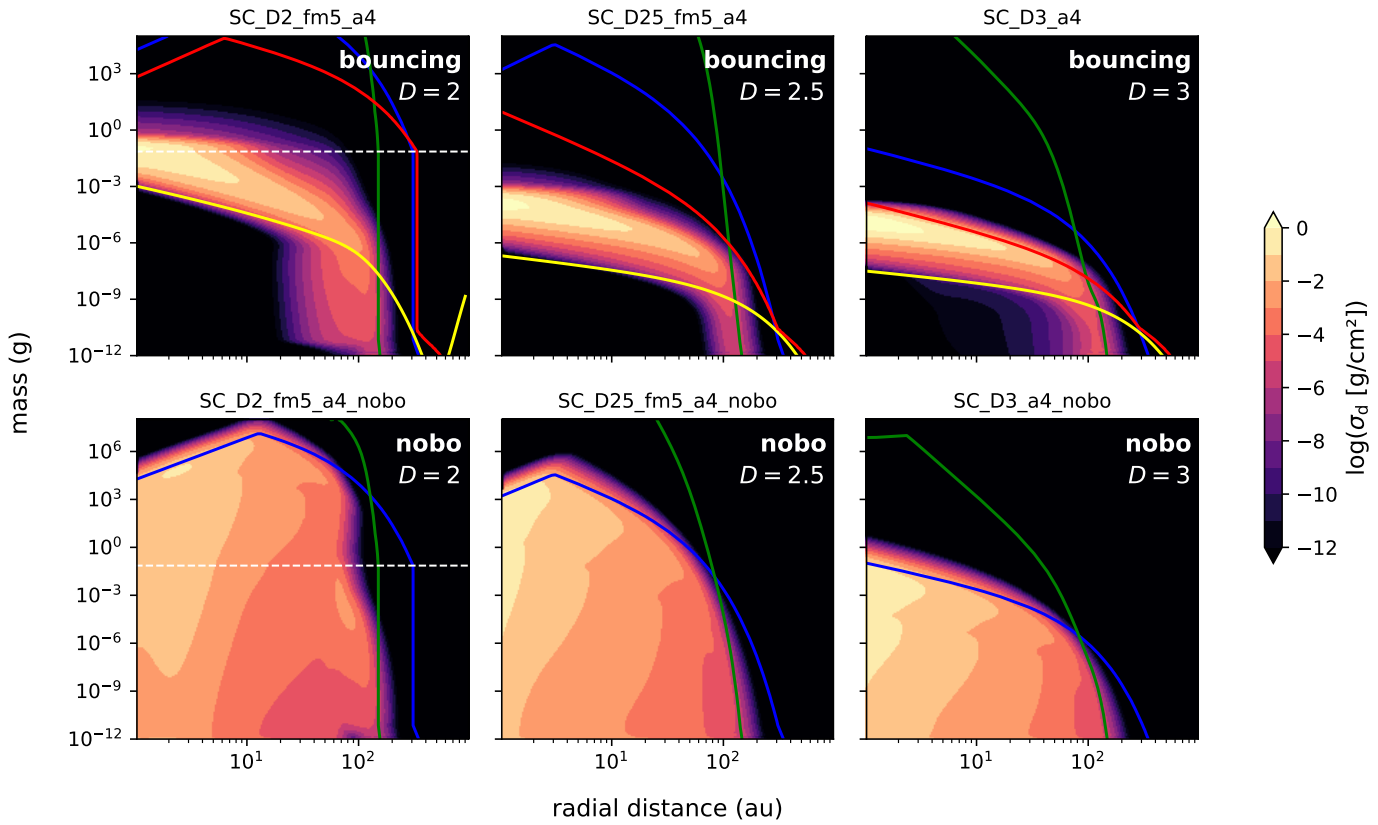

Fig. 3: Dust distributions of the SC models after 10^6 years with bouncing (upper row) and without bouncing (lower row) for different fractal dimensions. The green, blue, red and yellow lines show the analytical estimates of the drift, fragmentation, bouncing, and lower bouncing barrier, respectively. The dashed white lines indicate the transition from the fractal to the nonfractal growth regime. For $D = 2.5$, this transition lies outside the shown mass range.

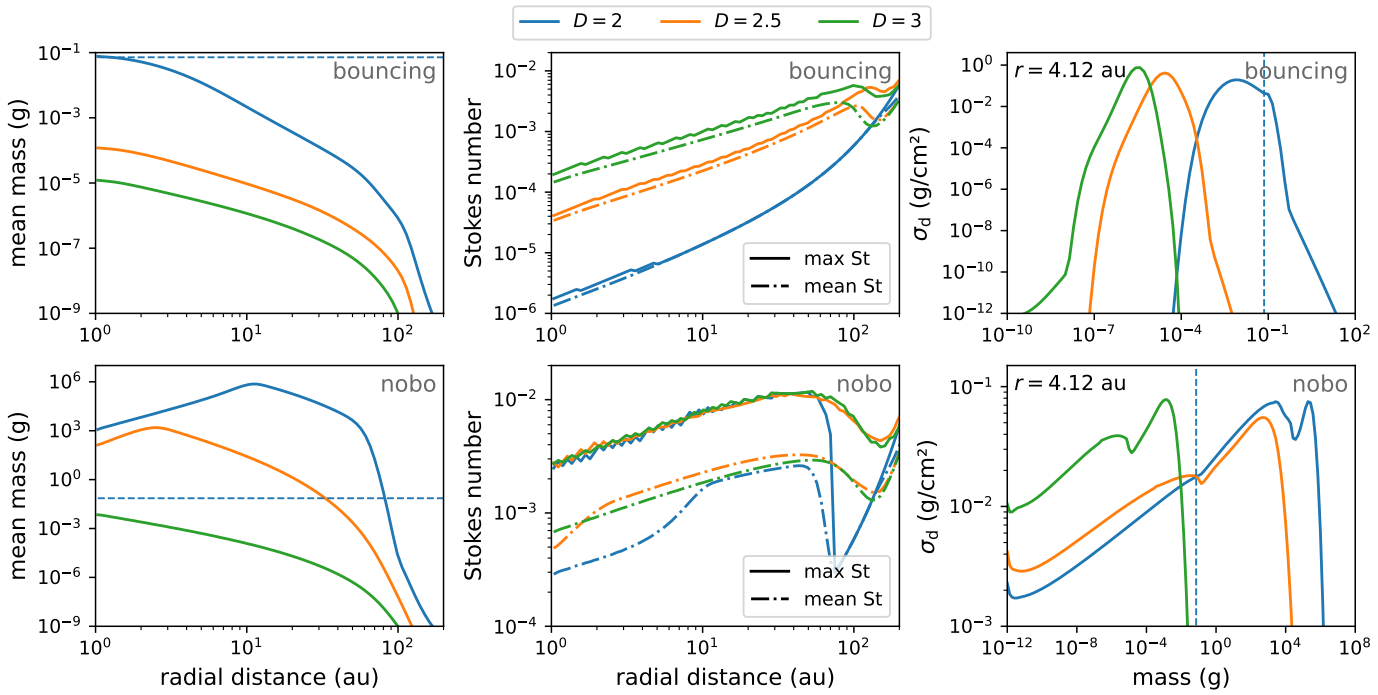

Fig. 4: Mean mass (left), maximum and mean Stokes numbers (middle), and a radial slice at $r = 4.12$ au (right) of the mass distribution after 10^6 years for different fractal dimensions of the models with bouncing (upper row) and without bouncing (lower row). The dashed blue lines in the right panels indicate the transition from fractal to nonfractal growth for the $D = 2$ models. For $D = 2.5$, this transition lies outside the shown mass range.

3.3.1. Dust distribution

The dust distributions σ_d after 10^6 years are shown in Fig. 3. For the definition of σ_d, see Appendix B. As predicted by analytical estimates, the dust distributions reach larger masses for smaller fractal dimensions (see also left panels of Fig. 4).

It also becomes clear from Fig. 3 that the analytical estimate overestimates the mass of the bouncing barrier for $D<3$. For the analytical estimate, it was assumed that the bouncing velocity is only exceeded when the larger particle leaves the $t_s < t_\eta$ regime. However, fractal particles can have rather large masses and still be in the $t_s < t_\eta$ regime. Since the bouncing velocity decreases with mass, it is already exceeded in the $t_s < t_\eta$ regime (if the mass ratio is not too large) despite the comparatively small relative velocities. It should also be noted that for $D = 3$ the bouncing velocity is already exceeded in the $t_s < t_\eta$ regime for collisions between similar masses. This suggests that collisions between particles with a large difference in mass play a role such that the particles can still grow further. The agreement of the estimate with the upper edge of the mass distribution in the numerical results for $D = 3$ might therefore be a coincidence. Since the assumption of similar-sized collisions is not valid, we have to consider both masses for the bouncing velocity. Furthermore, in the $t_s < t_\eta$ regime the relative velocities depend on both Stokes numbers. Therefore, it is hard to come up with a good estimate for the bouncing barrier. In contrast, the estimate for the lower bouncing barrier works reasonably well.

For models without bouncing, the particles can grow up to the fragmentation barrier. Since the fragmentation barrier lies outside the $t_s < t_\eta$ regime for all fractal dimensions, the estimate of the fragmentation barrier works well.

For $D = 2$ and $D = 2.5$, there is a kink in the fragmentation barrier at $r \sim 10$ au and $r \sim 4$ au, respectively. The reason is that the largest particles reach the Stokes drag regime in the inner parts of the disk. In the Stokes regime, the difference between the fragmentation barriers of the $D=2$ and $D=2.5$ models and the difference in mean mass is much smaller than in the Epstein regime, because the Stokes number, which is the relevant quantity that determines the fragmentation barrier, depends more weakly on the filling factor in the Stokes regime than in the Epstein regime (for a fixed mass, $\mathrm{St}^{\mathrm{Ep.}} \propto \phi^{2/3}$ and $\mathrm{St}^{\mathrm{St.}} \propto \phi^{1/3}$, which can be derived by exploiting $\rho \propto \phi$ and $a \propto (m/\phi)^{1/3} \propto \phi^{-1/3}$). The qualitative shape of the fragmentation-limited mass distributions is similar for all fractal dimensions (see the lower right panel of Fig. 4), approximately following a power law.

3.3.2. Stokes number

As can be seen in the middle panels of Fig. 4, the maximum Stokes number reached by a fragmentation-limited dust distribution does not depend on the fractal dimension. Since $\mathrm{St_f}$ does not depend on particle properties (see Eq. (16)), the fact that larger masses are reached for smaller fractal dimensions can be understood as an effect of the Stokes number dependence on mass and fractal dimension. For smaller fractal dimensions, larger masses are necessary for the Stokes number to exceed $\mathrm{St_f}$.

In the bouncing-limited case, the mean and maximum Stokes numbers decrease with decreasing fractal dimension. In contrast to $\mathrm{St_f}$, $\mathrm{St_b}$ depends on the mass via the bouncing velocity (see Eq. (17)). Models with smaller fractal dimensions can reach larger masses because their Stokes numbers still stay smaller. However, the bouncing velocity decreases due to the larger masses; therefore, it is already exceeded at smaller Stokes numbers compared to models with larger fractal dimensions.

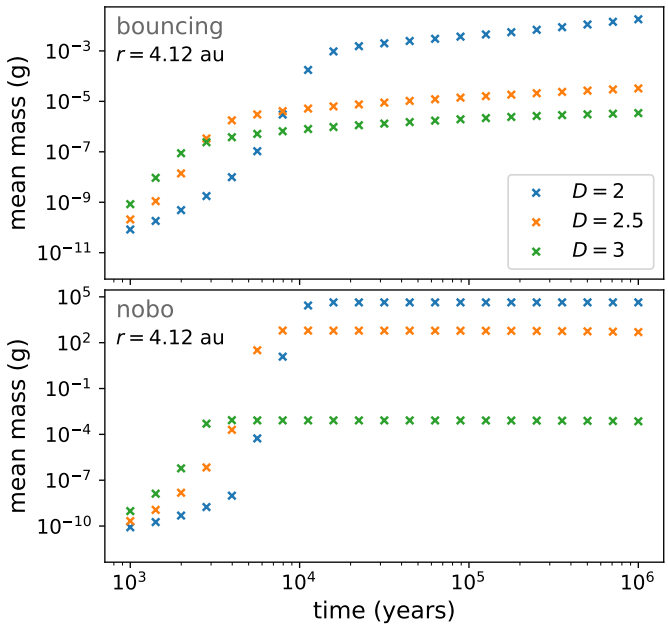

Fig. 5: Time evolution of the mean mass for the models with bouncing (top) and without bouncing (bottom) at $r = 4.1$ au.

3.3.3. Time evolution

Since the growth rate of dust particles depends on their collision cross section and relative velocity, which both depend on the fractal dimension, we expect that the time evolution of the dust distribution is influenced by the fractal dimension.

The growth rate is given by

$$\frac{\dot{m}}{m} = \int_{-\infty}^{\infty} \frac{R(m,m')}{m} \sigma_d(m') \mathrm{d}\log m', \tag{18}$$

with

$$\frac{R(m,m')}{m} = \frac{A_{\mathrm{coll}}(m,m')\, v_{\mathrm{rel}}(m,m')}{m\sqrt{2\pi}h(m')}. \tag{19}$$

Although the actual growth rate is given by Eq. (18), we refer to R/m as the growth rate in the following consideration.

We consider the case where Stokes numbers are in the Epstein regime, $\mathrm{St} \ll \alpha$ and $\mathrm{St} < \mathrm{St}_\eta = \mathrm{Re}^{-1/2}$. With the first condition, $A_{\mathrm{coll}}/m \propto \mathrm{St}^{-1}$, where we assumed $A_{\mathrm{coll}} \sim A_{\mathrm{aero}}$. With the second condition, we can approximate $h \approx H_P$. With the last condition, the relative velocities, which are typically dominated by vertical settling and turbulence, can be written as $v_{\mathrm{rel}} \propto \sqrt{\epsilon^2 \mathrm{St}^2 + (\mathrm{St} - \mathrm{St}')^2}$ (see Eqs. (A.11), (A.17), and (A.18)). Thus, the following relation approximately holds:

$$\frac{R}{m} \propto \sqrt{\epsilon^2 + \frac{(\mathrm{St} - \mathrm{St}')^2}{\mathrm{St}^2}}. \tag{20}$$

For smaller D, the term $\mathrm{St} - \mathrm{St}'$ is typically smaller; therefore, we expect the fractal particles to grow slower than the nonfractal particles, at least in the early phase of dust growth, where the above conditions are met.

When looking at the time evolution of the mean mass, shown in Fig. 5, growth is indeed slower for the fractal particles than nonfractal particles, as long as the particles are in the sticking regime, i.e., before the growth barriers are reached. Interestingly,

this is an apparent contradiction to previous studies that found that fractal growth is faster than nonfractal growth. In Sect. 5.3, we discuss how this discrepancy could be explained.

While growth is drastically slowed down but not fully stopped at the bouncing barrier, the fragmentation barrier stops growth completely. Due to the Maxwell-Boltzmann distribution of the relative velocities, there is a nonzero probability that the collision velocity is low enough for the collision to result in sticking, even if the mean relative velocity is above the threshold velocity for bouncing or fragmentation, respectively. At the bouncing barrier, larger particles that are produced in these sticking collisions stay large, even if they undergo many bouncing collisions afterwards. In contrast, larger particles that are produced at the fragmentation barrier get destroyed soon afterwards due to fragmentation (Dominik & Dullemond 2024).

3.4. Variation of the minimum filling factor

The minimum filling factor determines the bulk density of the particles once they reach the nonfractal growth regime. Thus, we expect the dust distribution to depend on $\phi_{\min}$ when the upper edge lies in the nonfractal growth regime.

Therefore, we varied the minimum filling factor. Since $\phi_{\min} = 10^{-5}$ is already a rather low value, we investigated larger values $\phi_{\min} = 10^{-4}$ and $\phi_{\min} = 10^{-3}$. For $D = 2.5$, even the comparatively large value $\phi_{\min} = 10^{-3}$ is only reached at $m \approx 7 \times 10^3$ g, which is just below the fragmentation barrier. Thus, we did not expect a considerable influence of $\phi_{\min}$ on the results of the $D = 2.5$ models and limited our investigation to the $D = 2$ models.

The mean mass and the maximum Stokes number are shown in Fig. 6. Increasing the minimum filling factor shifts the transition to the nonfractal growth regime towards smaller masses. In the outer disk regions, the mean mass is still within the fractal growth regime for the models with bouncing, therefore, there is no significant difference in mean mass. In the inner parts of the disk, when the mean mass is in the nonfractal growth regime, the models with larger $\phi_{\min}$ have smaller mean masses. In the case without bouncing, all models reach the nonfractal growth regime in the whole disk and the mean mass is smaller for models with larger $\phi_{\min}$. The lower right panel of Fig. 6 shows that the fragmentation barrier in terms of the Stokes number does not depend on $\phi_{\min}$. Thus, the difference in mean mass can again be understood as a consequence of the Stokes number dependence on mass and the filling factor. The maximum Stokes number reached by the models with bouncing decreases with increasing $\phi_{\min}$. As in Sect. 3.3, this can be attributed to the mass-dependence of the bouncing velocity.

3.5. Variation of the turbulent viscosity parameter

Many relevant processes and quantities depend on the turbulent viscosity parameter α. In particular, vertical settling and turbulent contributions to relative velocities depend on α. The influence of the viscosity parameter on dust evolution is investigated in several studies (e.g., Brauer et al. 2008; Estrada et al. 2022; Dominik & Dullemond 2024). Here, we want to focus our investigation on how the reaction to a change in the turbulent viscosity parameter α depends on the fractal dimension.

We therefore ran high turbulence models with $\alpha = 10^{-3}$, and low turbulence models with $\alpha = 10^{-6}$, each for different fractal dimensions. Note that the model SC_D2_fm5_a3_nobo had a glitch at about $t \sim 3.5 \times 10^5$ years, where the dust surface density dropped to zero in the inner part of the disk. However, the dust distribution reassembled again and the dust distribution at the end of the simulation after 10^6 years looks reasonable.

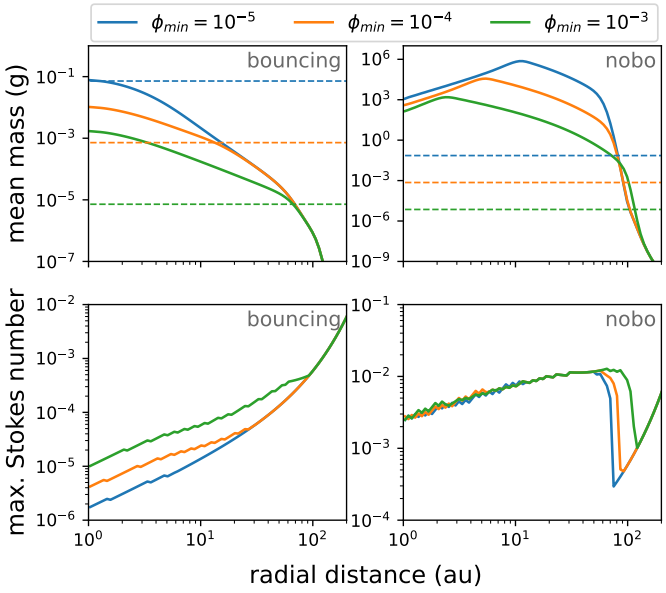

Fig. 6: Variation of the minimum filling factor for the $D = 2$ models. Upper row: Mean mass. Lower row: Maximum Stokes number. Left: Models with bouncing. Right: Models without bouncing.

For the mean mass, the general behavior is the same for all fractal dimensions. Since the relative velocities increase with the degree of turbulence, we expect that the growth barriers shift towards smaller masses for larger α, which is indeed the case for all fractal dimensions (see the left panels of Fig. 7).

The middle panels of Fig. 7 show the maximum Stokes numbers. The maximum Stokes number of the models with bouncing decreases with increasing turbulence for $D = 3$ and $D = 2.5$, although the decrease is only small for $D = 2.5$. For $D = 2$, the maximum Stokes number does not depend on α. Reaching the bouncing barrier already in the fractal growth regime for $D = 2$ is solely an effect of the decrease in the bouncing velocity with mass, as the Stokes number and, therefore, the relative velocities stay constant with mass. Increasing the turbulence parameter does not have an effect on the Stokes number but on the relative velocities, which are increased. Therefore, the bouncing velocity does not have to decrease as much as for low turbulence, and is therefore exceeded already at smaller masses. However, since the Stokes number is constant in mass, this does not change the Stokes number at which the relative velocities are exceeded.

For the shape of the mass distribution (right panels in Fig. 7), the behavior for different α depends on the fractal dimensions. First, we look at the models with bouncing. For the nonfractal case $D = 3$, the mass distribution of the high turbulence model extends down to the lower bound of the mass domain as for models without bouncing. The reason is that the fragmentation barrier is close to the bouncing barrier, such that some collisions already result in fragmentation (see Fig. D.1). For $D = 2.5$, the same is true for the outer parts of the disk but in the inner parts the growth is stopped by the bouncing barrier already well below the fragmentation barrier. For $D = 2$, this is true for the whole disk. Thus, when growth is bouncing limited, it is more difficult to still produce small particles for fractal models than for nonfractal models. The models without bouncing also show

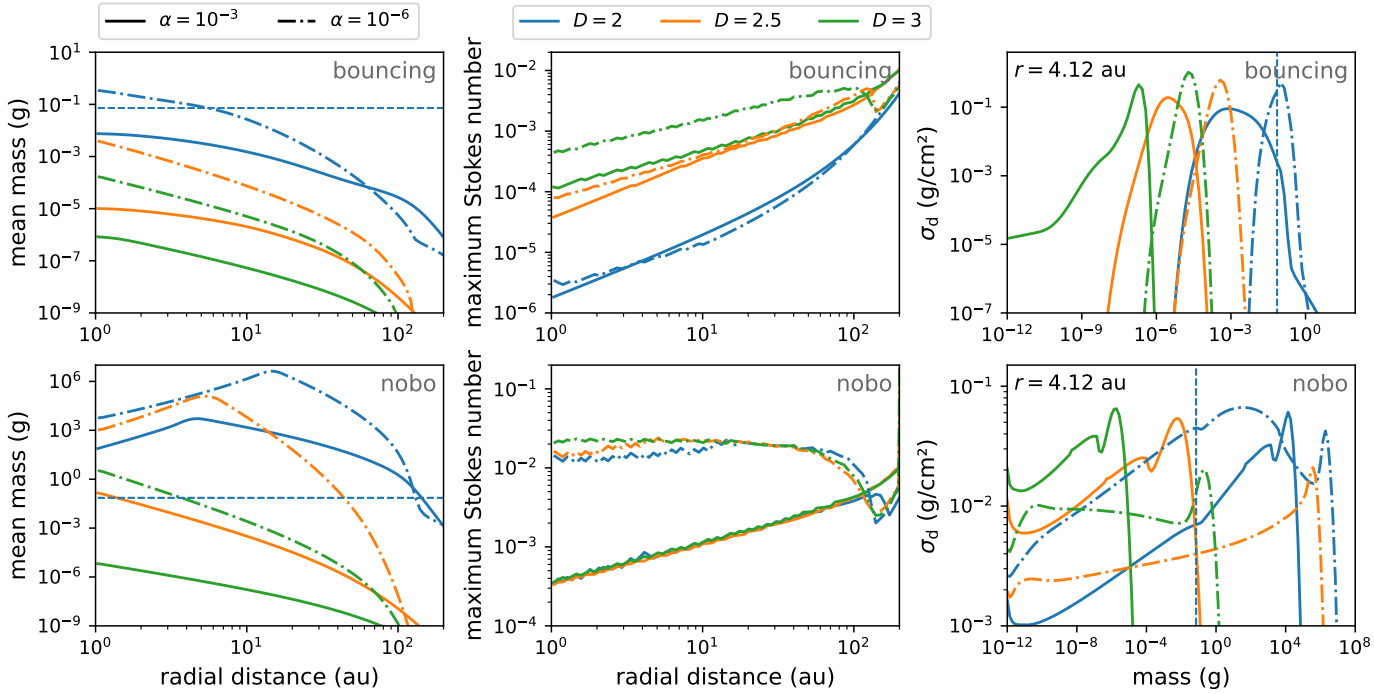

Fig. 7: Mean mass (left), maximum Stokes number (middle), and a radial slice at $r = 4.1$ au of the dust distribution for high ($\alpha = 10^{-3}$; solid lines) and low turbulence ($\alpha = 10^{-6}$; dash-dotted lines). The dashed blue lines in the left panels indicate the transition from the fractal to the nonfractal growth regime. For $D = 2.5$, this transition lies outside the shown mass range.

a peculiar behavior. For $D = 2.5$ and $D = 3$, the slope of $\sigma_d(m)$ becomes flatter when α is decreased. For $D = 3$, the slope is even slightly negative. For $D = 2$, there is no such effect. However, in all cases, the slopes are very flat.

4. Advanced cross sections

In Sect. 3, we applied a simple expression for the aerodynamical cross sections. Since this is a major simplification, we investigated how the results change for the different fractal dimensions if more elaborate expressions are applied. We refer to these models as advanced cross section (AC) models. In Sect. 4.1, we describe the advanced porosity model. Then, we compare the results of the AC models to those of the SC models for different fractal dimensions in Sect. 4.2.

4.1. Porosity model

Tazaki (2021) derives semi-analytical expressions for the aerodynamical cross sections of fractal particles

$$A_{\mathrm{T21}} = N\pi a_\bullet^2 \begin{cases} 12.5N^{-0.315}\exp\left(-\dfrac{2.53}{N^{0.0920}}\right) & \text{for } 1 \le N < N_{\mathrm{th}}, \\ \dfrac{\chi}{1+(N-1)\tilde{\sigma}} & \text{for } N_{\mathrm{th}} \le N, \end{cases} \tag{21}$$

where $N_{\mathrm{th}} = \min(11D - 8.5, 8.0)$ is a threshold below which the cross section does not depend on the aggregation process and therefore not on the fractal dimension. χ is a normalization factor connecting the $N < N_{\mathrm{th}}$ and the $N \ge N_{\mathrm{th}}$ regime, and $\tilde{\sigma}$ is the overlapping efficiency, given by (Tazaki 2021)

$$\tilde{\sigma} = \frac{\eta^{2/D}}{16}\int_\eta^\infty x^{-2/D}\exp(-x)\mathrm{d}x, \tag{22}$$

where $\eta = 2^{D-1}k_0/N$ and $k_0 = 0.761(1-D) + \sqrt{3}$.

Unfortunately, the simple expression of Eq. (14) cannot simply be replaced by Eq. (21) while leaving everything else unchanged. The reason is the following. Using the aerodynamical cross sections given by Eq. (21), together with the definition of radius as described by Eq. (11) and the expression for the collision cross sections given by Eq. (13), would imply that the aerodynamical cross sections of one particle can be larger than its collision cross section with a small collision partner. This is unphysical because the aerodynamical cross section corresponds to the collision cross section with a negligibly small collision partner (a gas molecule) and therefore always has to be smaller than the collision cross section with a collision partner of finite size.

The reason for this discrepancy is that Eq. (21) implies that initially all particles grow with a rather low actual fractal dimension D', and approach the given fractal dimension D only at larger sizes. For example, even a $D = 3$ aggregate gains some porosity initially (for $N \lesssim 10^3$) and only then proceeds to grow with constant porosity.

Thus, to keep the model consistent when using the aerodynamical cross sections given by Eq. (21), we have to redefine the radius of a fractal particle. We chose to take the area-equivalent radius. The full expression for the radius as a function of mass is then given by

$$a(m) = \begin{cases} a_\bullet\left(\dfrac{m}{m_\bullet}\right)^{1/3} & \text{for } m < m_\bullet, \\ \sqrt{A_{\mathrm{T21}}(m)/\pi} & \text{for } m_\bullet \le m \le m_{\mathrm{mff}}, \\ a_\bullet\phi_{\mathrm{min}}^{-1/3}\left(\dfrac{m}{m_\bullet}\right)^{1/3} & \text{for } m_{\mathrm{mff}} < m, \end{cases} \tag{23}$$

where m_{mff} is the mass at which the minimum filling factor is reached.

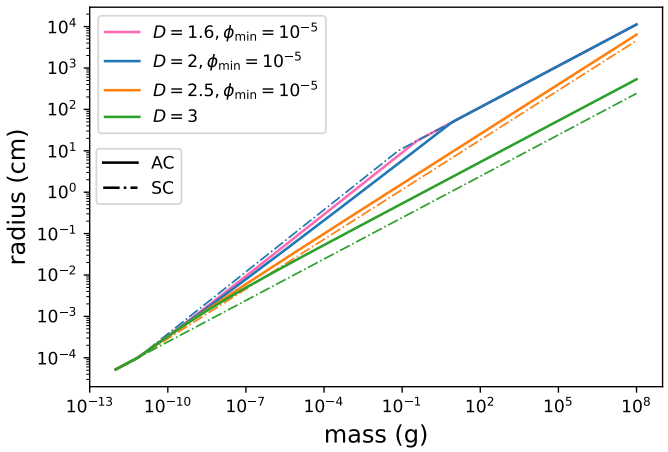

Fig. 8: Mass-radius relations of the AC models. For comparison, the SC models are also plotted as dash-dotted lines.

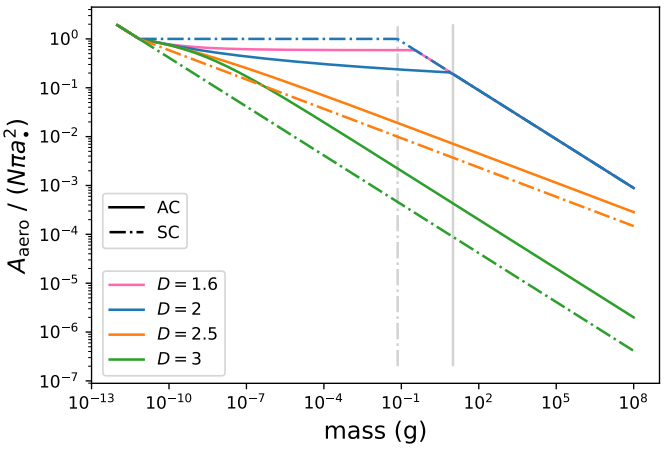

Fig. 9: Comparison between aerodynamical cross sections of the AC models (solid lines) and the SC models (dash-dotted lines). The cross sections are normalized to the sum of the monomer cross sections, $N\pi a_\bullet^2$. The vertical lines indicate the transition to nonfractal growth for the $D = 2$ models.

Table 2: Properties of the AC models.

Model name	D	$\phi_{\min}$	α	bo.?
AC_D3_a4	3	-	10^{-4}	yes
AC_D25_fm5_a4	2.5	10^{-5}	10^{-4}	yes
AC_D2_fm5_a4	2	10^{-5}	10^{-4}	yes
AC_D16_fm5_a4	1.6	10^{-5}	10^{-4}	yes
AC_D3_a4_nobo	3	-	10^{-4}	no
AC_D25_fm5_a4_nobo	2.5	10^{-5}	10^{-4}	no
AC_D2_fm5_a4_nobo	2	10^{-5}	10^{-4}	no
AC_D16_fm5_a4_nobo	1.6	10^{-5}	10^{-4}	no

Notes. Same as Table 1 but for the AC models. The model names are constructed in the same way, except that they start with AC instead of SC.

The advantage of this choice is that all the complications are absorbed into the definition of the radius. Consequently, the aerodynamical cross section can still be expressed as $A_{\rm aero} = \pi a^2$ and the expression for the Stokes number (see Eq. (4)) also stays the same. The collision cross section might be underestimated for large collision partners, but for small collision partners, it approaches the aerodynamical cross section, which is what one would expect.

The filling factor is then given by

$$\phi = \begin{cases} 1 & \text{for } m < m_\bullet, \\ \max\left[\dfrac{3m\sqrt{\pi}}{4A_{\rm T21}(m)^{3/2}\rho_{\rm s}}, \phi_{\min}\right] & \text{else.} \end{cases} \quad (24)$$

We refer to models using the porosity prescription described above as the advanced cross section (AC) models. The mass-radius relations of the AC models are shown in Fig. 8.

4.2. Comparison between AC and SC models

To investigate the effect of using the advanced cross section expressions, we ran eight AC models with $\phi_{\min} = 10^{-5}$, $\alpha = 10^{-4}$, and different fractal dimensions both with and without bouncing. The models and their properties are listed in Table 2.

Figure 9 compares the advanced cross sections with the simple cross sections. For $D = 3$ and $D = 2.5$ the advanced cross sections are larger than the simple cross sections. This is because the actual fractal dimension in the AC models is initially smaller than the given fractal dimension (see Sect. 4.1). For simple cross sections with $D = 2$, $A_{\rm aero}/(N\pi a_\bullet^2) = 1$. Hence, the cross section of the aggregate is exactly equal to the sum of the cross sections of all monomers of which the aggregate consists, which corresponds to the maximum cross section possible. Thus, there is no overlap of monomer cross sections, such that one monomer would insulate parts of another monomer from the gas flow. Instead, all monomers fully face the gas flow.

In the case of the advanced cross section, such overlapping effects are considered (for details, see Tazaki 2021). The total cross section of the aggregate is, therefore, somewhat smaller than the sum of the cross sections of all monomers. For this reason, the values $D < 2$ are also possible. Decreasing D below 2 makes overlapping less efficient and the cross sections get closer to the maximum possible cross section $N\pi a_\bullet^2$, which corresponds to the simple cross section with $D = 2$.

Figure 10 shows the comparison of the maximum Stokes number and the mean mass between the AC and SC models. In the fragmentation-limited case, the maximum Stokes numbers reached by the particles are independent of the cross-sectional model because the fragmentation barrier is only determined by the Stokes number. For $D = 2$, the mean mass is also independent of the cross-sectional model (except in the very outer part of the disk), because the fragmentation barrier lies in the nonfractal growth regime for $D = 2$, where the advanced and simple cross sections do not differ. For $D = 2.5$, the difference in mean mass is very small in the inner parts of the disk, where the particles are in the Stokes regime. In the outer parts of the disk, the mean mass of the AC model is $\sim 20\times$ larger. For $D = 3$, the difference is about a factor of ~ 100. In both cases, the difference in mean mass is an effect of the difference in the mass dependence of the Stokes numbers between the AC and SC models. In the Epstein regime, $\mathrm{St} \propto N/A_{\rm aero}$, therefore, the mass differences between the AC and SC models for a given $A_{\rm aero}/N$, which can be read from Fig. 9, correspond to the mass differences of the fragmentation-limited distribution.

In the bouncing-limited case, the behavior of the mean mass and the maximum Stokes number depends on the fractal dimension. In the case of $D = 2$, for a fixed mass, the advanced cross

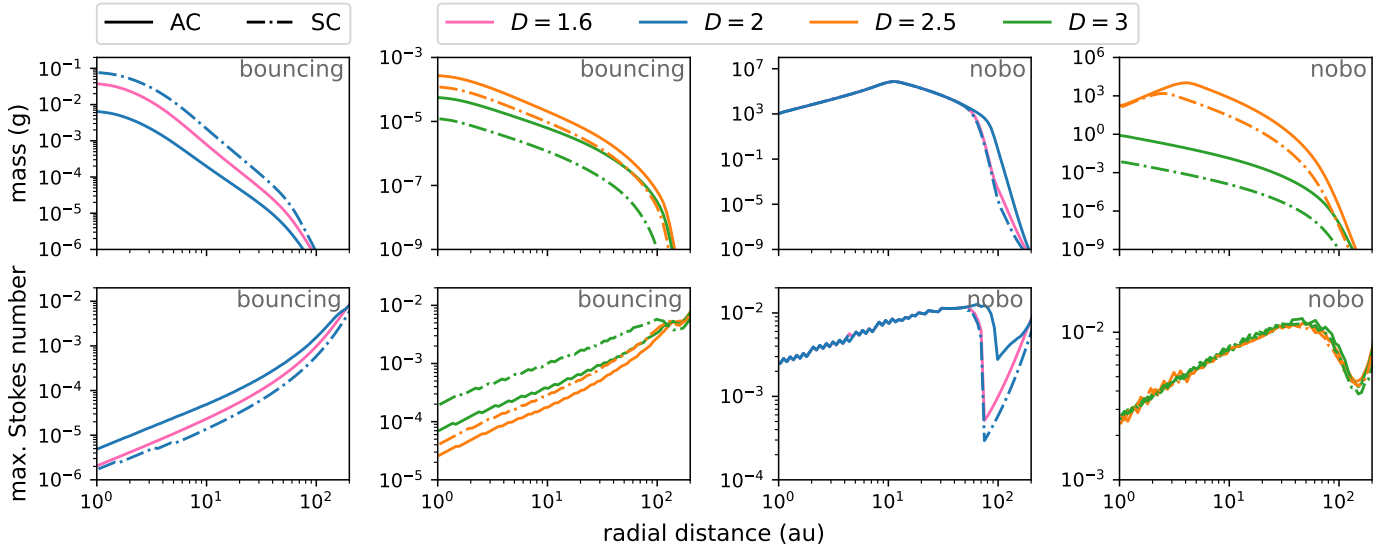

Fig. 10: Comparison between AC models (solid lines) and SC models (dash-dotted lines) for different fractal dimensions. Upper row: Mean mass. Lower row: Maximum Stokes number. Left: Models with bouncing. Right: Models without bouncing. For better visibility, we have drawn the models with $D \leq 2$ and $D > 2$ into different panels.

sections are smaller than the simple cross sections. Thus, despite the same value of D, the AC models can be viewed as having a "lower fractality" than the SC models. As already shown in Sects. 3.3 and 3.4, this leads to smaller masses for the AC models but larger maximum Stokes numbers due to the mass dependence of the bouncing velocity. For $D = 2.5$ and $D = 3$, the AC models have a "higher fractality" than the SC models and therefore reach larger masses but smaller maximum Stokes numbers. In all cases, decreasing the fractal dimension of the AC models from $D = 2$ to $D = 1.6$, decreases the difference to the SC model with $D = 2$.

5. Discussion

In the following, we discuss some aspects of our models and the results. First, we discuss how fractal growth changes the Stokes numbers that are reached at the end of the simulation, and what the implications are in the context of the streaming instability. Then, we discuss our finding that growth becomes slower with smaller fractal dimensions and try to explain the differences with previous studies.

5.1. Bouncing and fragmentation velocities

Due to the large uncertainties in the collision behavior of porous particles, and to keep things simple, we assumed that the collision outcome is not affected by the filling factor. Our expression for the bouncing velocity (Eqs. (6) and (5)) is based on the model of Güttler et al. (2010), where the bouncing velocity decreases with mass. This behavior is also found in more recent laboratory (e.g., Schräpler et al. 2022) and numerical (e.g., Oshiro et al. 2025) studies, although the exact mass dependence of v_b is somewhat different.

Our assumption that the collision outcome does not depend on the filling factor is a major simplification. Oshiro et al. (2025) investigate the bouncing behavior of porous aggregates numerically and find that the bouncing velocity increases with decreasing filling factor. Other numerical studies suggest that bouncing does not occur if the filling factor of a particle is below $\sim 0.3-0.4$ (Wada et al. 2011; Seizinger & Kley 2013), while laboratory studies still find bouncing for lower filling factors (e.g., Blum & Münch 1993; Langkowski et al. 2008; Schräpler et al. 2022). This discrepancy might be solved by a size dependency on the threshold filling factor (Arakawa et al. 2023). It should be noted that the filling factors explored in these laboratory experiments are still much larger than the filling factors reached in this study.

An increasing bouncing threshold velocity for decreasing filling factors would lead to even larger masses for fractal particles in bouncing-limited mass distributions, and the effect of smaller maximum Stokes numbers for smaller fractal dimensions would be reduced or even reversed, depending of the exact dependence of the bouncing velocity on the filling factor. A critical filling factor below which bouncing does not occur would lead to either a fragmentation-limited mass distribution if the critical filling factor is reached before the bouncing barrier or to a bouncing-limited mass distribution if the bouncing barrier is reached before the critical filling factor.

The fragmentation velocity might also depend on the fractal dimension or filling factor. Wada et al. (2009) find that the fragmentation velocity decreases by a factor of 2 when the fractal dimension decreases from $D = 3$ to $D = 2$. Gunkelmann et al. (2016) find that for a fixed mass, the fragmentation velocity decreases with decreasing filling factor for $\phi \lesssim 0.1$. It should be noted that the threshold velocities above which fragmentation occurs in these studies are on the order of a few 10 m/s, i.e., much larger than the fragmentation velocity assumed in this study.

A decreasing fragmentation velocity with decreasing fractal dimension would reduce the effect that smaller fractal dimensions reach larger masses and would lead to a decrease of maximum Stokes number for small fractal dimensions.

5.2. Streaming instability

We showed that with our choice of the fragmentation velocity $v_\mathrm{f} = 100$ cm s^{-1} particles cannot reach planetesimal masses even if their growth is highly fractal. Therefore, other mechanisms such as the streaming instability (Youdin & Goodman

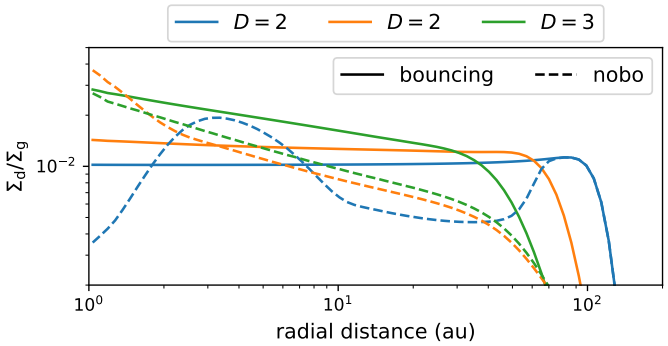

Fig. 11: Dust-to-gas ratio of the SC models with bouncing (solid) and without bouncing (dashed) for different fractal dimensions.

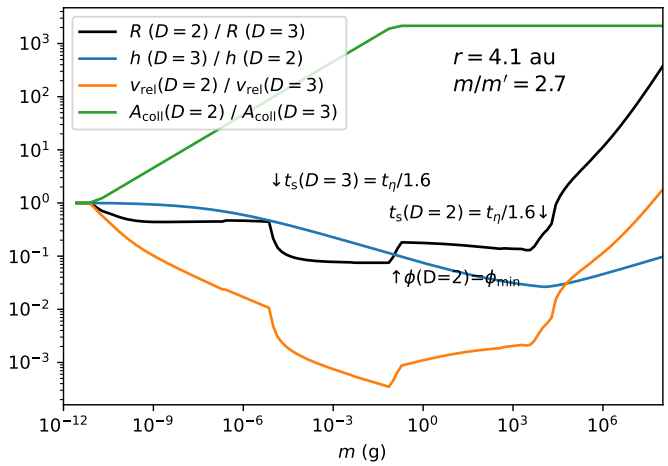

Fig. 12: Contributions of the settling factor (blue), the relative velocity (orange), and the collision cross section (green) to the ratio of the growth rates R (black) between the SC models with $D = 2$ and $D = 3$ for a mass ratio of 2.7.

2005; Johansen & Youdin 2007; Johansen et al. 2007) must be invoked to explain the formation of planetesimals. Studies have found that Stokes numbers must exceed $\mathrm{St} \sim 10^{-3}$ for the streaming instability to occur (Carrera et al. 2015; Yang et al. 2017; Li & Youdin 2021). The exact value depends on the dust-to-gas ratio Σ_d/Σ_g, which generally has to be $\gtrsim 0.005$ (Li & Youdin 2021) or $\gtrsim 0.01$ (Carrera et al. 2015; Yang et al. 2017).

For models with bouncing, the dust-to-gas ratio is somewhat larger for larger fractal dimensions because radial drift is more efficient and dust drifting inward from the outer regions increases the dust-to-gas ratio in the inner regions. For models without bouncing, the picture is less distinct. However, the dust-to-gas ratios are similar for all fractal dimensions except in the inner regions ($r \lesssim 3$ au), where the dust-to-gas ratio of the model with $D = 2$ is significantly lower (see Fig. 11). Note that the dust-to-gas ratio can be enhanced by dust traps (e.g., Kretke & Lin 2007; Dullemond et al. 2018), which we do not include in this study.

As shown in Sect. 3.3, the maximum Stokes number that is reached does not depend on the fractal dimension in the fragmentation-limited case. For all fractal dimensions, the maximum Stokes numbers are above 10^{-3}. In the bouncing-limited case, a lower fractal dimension even leads to smaller Stokes numbers. While maximum Stokes numbers of the models with $D = 3$ and $D = 2.5$ reach the threshold of 10^{-3} in the outer parts of the disk, the maximum Stokes numbers of the model with $D = 2$ are much smaller than 10^{-3} in the whole disk. Thus, under the assumption that the effect of fractal growth on the bouncing and fragmentation threshold velocities is negligible, fractal growth is not beneficial for the streaming instability in the fragmentation-limited case and even disadvantageous in the bouncing-limited case. However, as discussed in Sect. 5.1, the bouncing velocity might be higher for fractal particles, or bouncing might not occur below a critical filling factor. In this case, fractal growth could be less disadvantageous or even beneficial for the streaming instability. If the fragmentation threshold velocity was somewhat lower for fractal particles, fractal growth would be disadvantageous for the streaming instability in the fragmentation-limited case.

5.3. Fractal growth rate

We found that starting with the same initial mass distribution, particles in a model with a large fractal dimension will reach larger masses in a certain amount of time than the particles in a model with a small fractal dimension. This is in contrast to the results of previous studies that found that fractal or porous particles grow faster (Dullemond & Dominik 2005; Okuzumi et al. 2012; Estrada et al. 2022; Michoulier et al. 2024). Although Okuzumi et al. (2012) focus on the growth timescales in the Stokes regime, the fractal particles in their models grow somewhat faster than the nonfractal counterparts already in the Epstein regime (see their Fig. 4 and Fig. 7). In the following, we discuss the different results in our study and other studies.

When comparing the growth rate for two different fractal dimensions, several counteracting effects play a role. For a smaller fractal dimension, the collision cross section becomes larger, which increases the growth rate, but at the same time the relative velocities become lower (as long as $\mathrm{St} < 1$) and the dust scale height becomes larger, which decreases the growth rate.

Figure 12 shows how the different effects contribute to the total ratio between the growth rates of the models with $D = 3$ and $D = 2$. For small masses, the combined effect of relative velocity and settling is slightly stronger than the cross section effect, consistent with Eq. (20). However, this might be very sensitive to the model specifics, since the cross section effect and the relative velocity effect almost cancel out. Somewhat different treatments of settling, relative velocities, or collision cross sections than in our model might let the cross section effect become slightly larger than the relative velocity and settling effect, such that fractal particles would grow faster than nonfractal particles. When the nonfractal model leaves the $t_s < t_\eta$ regime (due to a transition regime, this already happens at $t_\eta/1.6$), the relative velocity increases, which intensifies the relative velocity difference between $D = 2$ and $D = 3$. When the $D = 2$ model reaches the nonfractal growth regime, the difference in relative velocities decreases again. When the $D = 2$ model leaves the $t_s < t_\eta$ regime, its relative velocities rapidly increase, and consequently, the growth rate becomes larger than that of the $D = 3$ model. However, the $D = 3$ model reaches the growth barrier already at much smaller masses, such that the comparison of the growth rate in these mass regimes is not meaningful with regard to our models.

6. Conclusions

In this work, we have modeled dust growth, including a prescription for porosity of fractal dust particles, and investigated

the dust evolution for different degrees of fractality, i.e., for different fractal dimensions. We have run models with and without bouncing and we have applied two kinds of cross section: the cross section of a spherical particle, and a more advanced, semi-analytic expression. This leads us to the following conclusions:

- Decreasing the fractal dimension shifts the fragmentation and bouncing barriers towards larger masses. Therefore, models with smaller fractal dimensions reach larger masses, with and without bouncing.
- For a fragmentation-limited mass distribution, the maximum Stokes numbers that are reached do not depend on the fractal dimension. The mean Stokes numbers show a small dependence on the fractal dimension. Therefore, under the assumption that the fragmentation velocity does not depend on the fractal dimension or filling factor, fractal growth is not beneficial for the streaming instability in the case of a fragmentation-limited mass distribution.
- For a bouncing-limited mass distribution, both the maximum and mean Stokes numbers decrease with decreasing fractal dimension. Therefore, under the assumption that the bouncing velocity does not depend on the fractal dimension or filling factor, fractal growth is disadvantageous for the streaming instability in the case of a bouncing-limited mass distribution.
- Fractal growth is slower than nonfractal growth because the larger collision cross sections compensate for the smaller relative velocities and degree of vertical settling. However, the effect is only small. Changing the model specifics might lead to different results.
- In the high turbulence case ($\alpha = 10^{-3}$), the bouncing and fragmentation barriers are close together for nonfractal particles, so that some fragmentation events occur, although the bouncing is active. For moderately ($D = 2.5$) or highly fractal ($D = 2$) particles, this occurs only in the outer parts of the disk or not at all, respectively, because the bouncing and fragmentation barriers are further apart.
- Using more advanced expressions for the cross sections does not change the maximum Stokes number that the particles reach in the fragmentation-limited case, while it leads to larger maximum Stokes numbers for $D = 2$ and to smaller maximum Stokes numbers for $D = 2.5$ and $D = 3$. The masses reached with the advanced cross sections become smaller for $D = 2$ and larger for $D = 2.5$ and $D = 3$.
- The $D = 2$ case of the simple cross sections corresponds to the maximum possible cross sections. Highly fractal ($D < 2$) models with advanced cross sections therefore approach the $D = 2$ model with simple cross sections, as the fractal dimension decreases.

Acknowledgements. We acknowledge support by the High Performance and Cloud Computing Group at the Zentrum für Datenverarbeitung of the University of Tübingen, the state of Baden-Württemberg through bwHPC and the German Research Foundation (DFG) through grant INST 37/935-1 FUGG. Carsten Dominik acknowledges support from the ERC AdG project grant 101199769 GT4Pebbles.

References

Arakawa, S., Okuzumi, S., Tatsuuma, M., et al. 2023, ApJ, 951, L16
Beutel, M. & Dullemond, C. P. 2023, A&A, 670, A134
Birnstiel, T., Dullemond, C. P., & Brauer, F. 2009, A&A, 503, L5
Birnstiel, T., Klahr, H., & Ercolano, B. 2012, A&A, 539, A148
Blum, J. & Münch, M. 1993, Icarus, 106, 151
Blum, J. & Wurm, G. 2008, ARA&A, 46, 21
Brauer, F., Dullemond, C. P., & Henning, T. 2008, A&A, 480, 859
Carrera, D., Johansen, A., & Davies, M. B. 2015, A&A, 579, A43
Dominik, C. & Dullemond, C. P. 2024, A&A, 682, A144
Dominik, C. & Tielens, A. G. G. M. 1997, ApJ, 480, 647
Dubrulle, B., Morfill, G., & Sterzik, M. 1995, Icarus, 114, 237
Dullemond, C. P., Birnstiel, T., Huang, J., et al. 2018, ApJ, 869, L46
Dullemond, C. P. & Dominik, C. 2005, A&A, 434, 971
Estrada, P. R. & Cuzzi, J. N. 2008, ApJ, 682, 515
Estrada, P. R., Cuzzi, J. N., & Umurhan, O. M. 2022, ApJ, 936, 42
Gunkelmann, N., Ringl, C., & Urbassek, H. M. 2016, A&A, 589, A30
Güttler, C., Blum, J., Zsom, A., Ormel, C. W., & Dullemond, C. P. 2010, A&A, 513, A56
Güttler, C., Mannel, T., Rotundi, A., et al. 2019, A&A, 630, A24
Johansen, A., Oishi, J. S., Mac Low, M.-M., et al. 2007, Nature, 448, 1022
Johansen, A. & Youdin, A. 2007, ApJ, 662, 627
Kataoka, A., Tanaka, H., Okuzumi, S., & Wada, K. 2013a, A&A, 557, L4
Kataoka, A., Tanaka, H., Okuzumi, S., & Wada, K. 2013b, A&A, 554, A4
Kretke, K. A. & Lin, D. N. C. 2007, ApJ, 664, L55
Krijt, S., Ormel, C. W., Dominik, C., & Tielens, A. G. G. M. 2015, A&A, 574, A83
Langkowski, D., Teiser, J., & Blum, J. 2008, ApJ, 675, 764
Li, R. & Youdin, A. N. 2021, ApJ, 919, 107
Lorek, S., Lacerda, P., & Blum, J. 2018, A&A, 611, A18
Lynden-Bell, D. & Pringle, J. E. 1974, MNRAS, 168, 603
Mathis, J. S., Rumpl, W., & Nordsieck, K. H. 1977, ApJ, 217, 425
Michoulier, S., Gonzalez, J.-F., & Price, D. J. 2024, A&A, 688, A31
Okuzumi, S. 2009, ApJ, 698, 1122
Okuzumi, S., Tanaka, H., Kobayashi, H., & Wada, K. 2012, ApJ, 752, 106
Okuzumi, S., Tanaka, H., & Sakagami, M.-a. 2009, ApJ, 707, 1247
Okuzumi, S., Tanaka, H., Takeuchi, T., & Sakagami, M.-a. 2011, ApJ, 731, 95
Ormel, C. W. & Cuzzi, J. N. 2007, A&A, 466, 413
Ormel, C. W., Spaans, M., & Tielens, A. G. G. M. 2007, A&A, 461, 215
Oshiro, H., Tatsuuma, M., Okuzumi, S., & Tanaka, H. 2025, ApJ, 983, 75
Schräpler, R., Blum, J., Seizinger, A., & Kley, W. 2012, ApJ, 758, 35
Schräpler, R. R., Landeck, W. A., & Blum, J. 2022, MNRAS, 509, 5641
Seizinger, A. & Kley, W. 2013, A&A, 551, A65
Shakura, N. I. & Sunyaev, R. A. 1973, A&A, 24, 337
Smoluchowski, M. V. 1916, Zeitschrift fur Physik, 17, 557
Stammler, S. M. & Birnstiel, T. 2022, ApJ, 935, 35
Suyama, T., Wada, K., & Tanaka, H. 2008, ApJ, 684, 1310
Tanaka, H., Himeno, Y., & Ida, S. 2005, ApJ, 625, 414
Tazaki, R. 2021, MNRAS, 504, 2811
Wada, K., Tanaka, H., Suyama, T., Kimura, H., & Yamamoto, T. 2007, ApJ, 661, 320
Wada, K., Tanaka, H., Suyama, T., Kimura, H., & Yamamoto, T. 2008, ApJ, 677, 1296
Wada, K., Tanaka, H., Suyama, T., Kimura, H., & Yamamoto, T. 2009, ApJ, 702, 1490
Wada, K., Tanaka, H., Suyama, T., Kimura, H., & Yamamoto, T. 2011, ApJ, 737, 36
Weidenschilling, S. J. 1977, MNRAS, 180, 57
Weidenschilling, S. J. 1997, Icarus, 127, 290
Xiang, C., Matthews, L. S., Carballido, A., & Hyde, T. W. 2020, ApJ, 897, 182
Yang, C.-C., Johansen, A., & Carrera, D. 2017, A&A, 606, A80
Youdin, A. N. & Goodman, J. 2005, ApJ, 620, 459
Zsom, A. & Dullemond, C. P. 2008, A&A, 489, 931
Zsom, A., Ormel, C. W., Güttler, C., Blum, J., & Dullemond, C. P. 2010, A&A, 513, A57

Appendix A: Area dispersion

Two fractal particles of the same mass can have slightly different cross sections due to the statistical nature of their structure. We refer to this as area dispersion. To take into account the effect of area dispersion, we adjusted the expressions for relative velocities. In the following, we derive these adjusted expressions (Sect. A.1) and then investigate the effect of area dispersion (Sect. A.2).

A.1. Derivation of relative velocity expressions

Here, we derive the expressions for the relative velocities including area dispersion. We assume that for each mass bin, the mass-to-area ratio $B = m/A$ (and therefore the Stokes number) is dispersed following a Log-Gauss-distribution:

$$p(B)\mathrm{d}\ln B = \frac{1}{\sqrt{2\pi}\sigma}\exp\left[-\frac{(\ln(B/\mu^*))^2}{2\sigma^2}\right]\mathrm{d}\ln B, \tag{A.1}$$

where $\mu^* = \exp(\mu)$ and $\mu = \overline{\ln B}$ is the mean of $\ln B$ and σ is the standard deviation of $\ln B$. The dispersion of mass-to-area ratio leads to a dispersion of Stokes numbers. We include area dispersion into the relative velocity equations by feeding them with the distribution of Stokes numbers and then taking the root mean square.

We note that

$$\overline{B^x} = \overline{B}^x \exp\left(\frac{x^2 - x}{2}\sigma^2\right), \tag{A.2}$$

for an arbitrary exponent x. We assume that the mass-to-area ratios are not correlated between two particles, therefore $\overline{B_1 B_2} = \overline{B}_1\overline{B}_2$ holds.

Although we assume a Log-Gauss distribution, the results for radial drift, turbulence and, for $\mathrm{St} \ll \alpha$, vertical settling are more general. In this case, it is sufficient to assume that the variance can be written as

$$\mathrm{Var}(B) = \overline{B}^2\epsilon^2. \tag{A.3}$$

The reason is that $\overline{B^2}$ can be written as $\overline{B}^2 + \mathrm{Var}(B)$. Thus, it is not necessary to assume a particular distribution, as long as the mean and the variance are known. However, the results for azimuthal drift and the $\alpha \lesssim \mathrm{St}$ regime of vertical settling are less general, because higher powers of St appear, whose averages as a function of $\overline{\mathrm{St}}$ depend on the chosen distribution. For the Log-Gauss distribution, ϵ is given by

$$\epsilon^2 = \exp\left(\sigma^2\right) - 1. \tag{A.4}$$

To keep it general, we distinguish between the width parameter ϵ_1 and ϵ_2 for two different mass bins in the derivation. For our models, however, we assume that ϵ is the same for all mass bins.

A.1.1. Radial drift

The default expression for radial drift in `DustPy` is given by (Stammler & Birnstiel 2022)

$$v_{\mathrm{rel}}^{\mathrm{rad}} = \left|\frac{v_\mathrm{g} + 2v_{\mathrm{drift}}^{\max}\mathrm{St}_1}{1+\mathrm{St}_1^2} - \frac{v_\mathrm{g} + 2v_{\mathrm{drift}}^{\max}\mathrm{St}_2}{1+\mathrm{St}_2^2}\right|, \tag{A.5}$$

where v_g is the velocity of the gas, and

$$v_{\mathrm{drift}}^{\max} = \frac{1}{2}\left(\frac{H_P}{r}\right)^2\frac{\partial \ln P}{\partial \ln r}. \tag{A.6}$$

We approximate

$$\frac{\mathrm{St}}{1+\mathrm{St}^2} \approx \frac{\mathrm{St}}{1+\overline{\mathrm{St}^2}} = \frac{\mathrm{St}}{1+(1+\epsilon^2)\overline{\mathrm{St}}^2}.$$

The mean square is then given by

$$\overline{\left(v_{\mathrm{rel}}^{\mathrm{rad}}\right)^2} = \left(\frac{v_\mathrm{g} + 2v_{\mathrm{drift}}^{\max}\overline{\mathrm{St}}_1}{1+\left(1+\epsilon_1^2\right)\overline{\mathrm{St}}_1^2} - \frac{v_\mathrm{g} + 2v_{\mathrm{drift}}^{\max}\overline{\mathrm{St}}_2}{1+\left(1+\epsilon_2^2\right)\overline{\mathrm{St}}_2^2}\right)^2 + \epsilon_1^2\left(\frac{2v_{\mathrm{drift}}^{\max}\overline{\mathrm{St}}_1}{1+\left(1+\epsilon_1^2\right)\overline{\mathrm{St}}_1^2}\right)^2 + \epsilon_2^2\left(\frac{2v_{\mathrm{drift}}^{\max}\overline{\mathrm{St}}_2}{1+\left(1+\epsilon_2^2\right)\overline{\mathrm{St}}_2^2}\right)^2. \tag{A.7}$$

The first term in Eq. (A.7) looks similar to the original expression but there are additional terms which depend on the dispersion parameter ϵ.

A.1.2. Azimuthal drift

The default expression for relative velocities induced by azimuthal drift is given by (Stammler & Birnstiel 2022)

$$v_{\mathrm{rel}}^{\mathrm{azi}} = \left|v_{\mathrm{drift}}^{\max}\frac{\mathrm{St}_2^2 - \mathrm{St}_1^2}{\left(1+\mathrm{St}_1^2\right)\left(1+\mathrm{St}_2^2\right)}\right|. \tag{A.8}$$

We approximate

$$\left|\frac{\mathrm{St}_1^2 - \mathrm{St}_2^2}{\left(1+\mathrm{St}_1^2\right)\left(1+\mathrm{St}_2^2\right)}\right| \approx \left|\frac{\mathrm{St}_1^2 - \mathrm{St}_2^2}{\left(1+\overline{\mathrm{St}_1^2}\right)\left(1+\overline{\mathrm{St}_2^2}\right)}\right|.$$

The mean square of Eq. (A.8) is then given by

$$\overline{\left(v_{\mathrm{rel}}^{\mathrm{azi}}\right)^2} = v_{\mathrm{drift}}^{\max}\left(\frac{1}{1+\left(1+\epsilon_1^2\right)\overline{\mathrm{St}}_1^2} - \frac{1}{1+\left(1+\epsilon_2^2\right)\overline{\mathrm{St}}_2^2}\right)^2 + 5v_{\mathrm{drift}}^{\max}\frac{\epsilon_1^2\overline{\mathrm{St}}_1^4 + \epsilon_2^2\overline{\mathrm{St}}_2^4}{\left(1+\left(1+\epsilon_1^2\right)\overline{\mathrm{St}}_1^2\right)^2\left(1+\left(1+\epsilon_2^2\right)\overline{\mathrm{St}}_2^2\right)^2}, \tag{A.9}$$

where we neglected $O\left(\epsilon^4\right)$ terms.

A.1.3. Vertical settling

The default expression for vertical settling is given by (Stammler & Birnstiel 2022)

$$v_{\mathrm{rel}}^{\mathrm{sett}} = c_{\mathrm{s,iso}}\sqrt{\alpha}\left|\frac{\min(\mathrm{St}_1, 0.5)}{\sqrt{\alpha+\mathrm{St}_1}} - \frac{\min(\mathrm{St}_2, 0.5)}{\sqrt{\alpha+\mathrm{St}_2}}\right|, \tag{A.10}$$

where $c_{\mathrm{s,iso}} = c_\mathrm{s}/\sqrt{\gamma}$, is the isothermal sound speed.

First, we consider the case, where $\mathrm{St}_1, \mathrm{St}_2 < 0.5$. For $\mathrm{St} \ll \alpha$ we again neglect the area dispersion of the denominator:

$$\frac{\mathrm{St}}{\sqrt{\alpha+\mathrm{St}}} \approx \frac{\mathrm{St}}{\sqrt{\alpha+\overline{\mathrm{St}}}}.$$

For $\mathrm{St} \gg \alpha$, we rewrite the term

$$\frac{\mathrm{St}}{\sqrt{\alpha+\mathrm{St}}} = \frac{\sqrt{\mathrm{St}}}{\sqrt{1+\alpha/\mathrm{St}}},$$

where we can then again neglect the area dispersion of the denominator.

For $\mathrm{St}_1, \mathrm{St}_2 \ll \alpha$, the mean square of Eq. (A.10) is given by

$$\overline{\left(v_{\mathrm{rel}}^{\mathrm{sett}}\right)^2} = \alpha c_{\mathrm{s,iso}}^2 \left(\frac{\overline{\mathrm{St}_1}}{\sqrt{\alpha + \overline{\mathrm{St}_1}}} - \frac{\overline{\mathrm{St}_2}}{\sqrt{\alpha + \overline{\mathrm{St}_2}}} \right)^2 + \alpha c_{\mathrm{s,iso}}^2 \epsilon_1^2 \left(\frac{\overline{\mathrm{St}_1}}{\sqrt{\alpha + \overline{\mathrm{St}_1}}} \right)^2 + \alpha c_{\mathrm{s,iso}}^2 \epsilon_2^2 \left(\frac{\overline{\mathrm{St}_2}}{\sqrt{\alpha + \overline{\mathrm{St}_2}}} \right)^2 . \tag{A.11}$$

For $\mathrm{St}_2 \ll \alpha \ll \mathrm{St}_1$, the mean square of Eq. (A.10) is given by

$$\overline{\left(v_{\mathrm{rel}}^{\mathrm{sett}}\right)^2} = \alpha c_{\mathrm{s,iso}}^2 \left(\frac{\overline{\mathrm{St}_1}}{\sqrt{\alpha + \overline{\mathrm{St}_1}}} - \frac{\overline{\mathrm{St}_2}}{\sqrt{\alpha + \overline{\mathrm{St}_2}}} \right)^2 + \alpha c_{\mathrm{s,iso}}^2 \frac{\epsilon_1^2}{4} \frac{\overline{\mathrm{St}_1}}{\sqrt{\alpha + \overline{\mathrm{St}_1}}} \frac{\overline{\mathrm{St}_2}}{\sqrt{\alpha + \overline{\mathrm{St}_2}}} + \alpha c_{\mathrm{s,iso}}^2 \epsilon_2^2 \frac{\overline{\mathrm{St}_2^2}}{\alpha + \mathrm{St}_2}, \tag{A.12}$$

and vice versa for $\mathrm{St}_1 \ll \alpha \ll \mathrm{St}_2$. For $\alpha \ll \mathrm{St}_1, \mathrm{St}_2$, the mean square of Eq. (A.10) is given by

$$\overline{\left(v_{\mathrm{rel}}^{\mathrm{sett}}\right)^2} = \alpha c_{\mathrm{s,iso}}^2 \left(\frac{\overline{\mathrm{St}_1}}{\sqrt{\alpha + \overline{\mathrm{St}_1}}} - \frac{\overline{\mathrm{St}_2}}{\sqrt{\alpha + \overline{\mathrm{St}_2}}} \right)^2 + \frac{1}{4} \alpha c_{\mathrm{s}}^2 \left(\epsilon_1^2 + \epsilon_2^2 \right) \frac{\overline{\mathrm{St}_1}}{\sqrt{\alpha + \overline{\mathrm{St}_1}}} \frac{\overline{\mathrm{St}_2}}{\sqrt{\alpha + \overline{\mathrm{St}_2}}}. \tag{A.13}$$

To merge Eqs. (A.10), (A.12), and (A.13) together, we define coefficients

$$p = \frac{\alpha}{\overline{\mathrm{St}} + \alpha} \quad \text{and} \quad q = 1 - p.$$

Furthermore, to include the case $\mathrm{St} > 0.5$, we define coefficients

$$y = \begin{cases} 1 \text{ for } \mathrm{St} \leq 0.5, \\ 0 \text{ for } \mathrm{St} > 0.5, \end{cases}$$

and $z = 1 - y$. Putting everything together yields

$$\begin{aligned} \overline{\left(v_{\mathrm{rel}}^{\mathrm{sett}}\right)^2} = \alpha c_{\mathrm{s,iso}}^2 \Bigg[& \left(\frac{\min\left(\overline{\mathrm{St}_1}, 0.5\right)}{\sqrt{\alpha + \overline{\mathrm{St}_1}}} - \frac{\min\left(\overline{\mathrm{St}_2}, 0.5\right)}{\sqrt{\alpha + \overline{\mathrm{St}_2}}} \right)^2 \\ & + y_1 p_1 \epsilon_1^2 \frac{\overline{\mathrm{St}_1^2}}{\alpha + \overline{\mathrm{St}_1}} + y_2 p_2 \epsilon_2^2 \frac{\overline{\mathrm{St}_2^2}}{\alpha + \overline{\mathrm{St}_2}} \\ & + \left(y_1 q_1 \frac{\epsilon_1^2}{4} + y_2 q_2 \frac{\epsilon_2^2}{4} \right) \frac{\min\left(\overline{\mathrm{St}_1}, 0.5\right) \min\left(\overline{\mathrm{St}_2}, 0.5\right)}{\sqrt{\left(\alpha + \overline{\mathrm{St}_1}\right)\left(\alpha + \overline{\mathrm{St}_2}\right)}} \\ & + z_1 \epsilon_1^2 \left(\frac{0.25}{\alpha + \mathrm{St}_1} - \frac{3}{4} \frac{0.5 \min\left(\overline{\mathrm{St}_2}, 0.5\right)}{\sqrt{\left(\alpha + \overline{\mathrm{St}_1}\right)\left(\alpha + \overline{\mathrm{St}_2}\right)}} \right) \\ & + z_2 \epsilon_2^2 \left(\frac{0.25}{\alpha + \mathrm{St}_2} - \frac{3}{4} \frac{0.5 \min\left(\overline{\mathrm{St}_1}, 0.5\right)}{\sqrt{\left(\alpha + \overline{\mathrm{St}_2}\right)\left(\alpha + \overline{\mathrm{St}_1}\right)}} \right) \Bigg], \end{aligned} \tag{A.14}$$

where we assumed $\overline{\min(\mathrm{St}, 0.5)} = \min\left(\overline{\mathrm{St}}, 0.5\right)$. This is not always true but the deviations are small because $\epsilon \ll 1$.

The total relative velocity is given by the quadratic sum of the contributions:

$$v_{\mathrm{rel}}^{\mathrm{tot}} = \sqrt{\left(v_{\mathrm{rel}}^{\mathrm{brown}}\right)^2 + \left(v_{\mathrm{rel}}^{\mathrm{sett}}\right)^2 + \left(v_{\mathrm{rel}}^{\mathrm{rad}}\right)^2 + \left(v_{\mathrm{rel}}^{\mathrm{azi}}\right)^2 + \left(v_{\mathrm{rel}}^{\mathrm{turb}}\right)^2}. \tag{A.15}$$

A.1.4. Turbulence

For turbulence, `DustPy` differentiates between different turbulence regimes, based on the stopping time t_{L} of the larger particle. Only the first two regimes depend on the difference between Stokes numbers. The other regimes therefore do not have to be modified.

For $t_{\mathrm{L}} < 0.2 t_\eta$, the default equation is given by

$$v_{\mathrm{rel}}^{\mathrm{turb}} = \sqrt{\frac{3\alpha}{2}} \mathrm{Re}^{1/4} c_{\mathrm{s}} \left| \mathrm{St}_1 - \mathrm{St}_2 \right|. \tag{A.16}$$

The mean square of Eq. (A.16) is given by

$$\overline{\left(v_{\mathrm{rel}}^{\mathrm{turb}}\right)^2} = \frac{3\alpha}{2} \mathrm{Re}^{1/2} c_{\mathrm{s}}^2 \left[\left(\overline{\mathrm{St}_1} - \overline{\mathrm{St}_2}\right)^2 + \epsilon_1^2 \overline{\mathrm{St}_1^2} + \epsilon_2^2 \overline{\mathrm{St}_2^2} \right]. \tag{A.17}$$

For $0.2 t_\eta \leq t_{\mathrm{L}} < t_\eta / y_{\mathrm{a}}$, where $y_{\mathrm{a}} = 1.6$, the turbulent relative velocity is given by

$$v_{\mathrm{rel}}^{\mathrm{turb}} = \sqrt{\frac{3\alpha}{2}} c_{\mathrm{s}} \left[\frac{\mathrm{St_L} - \mathrm{St_S}}{\mathrm{St_L} + \mathrm{St_S}} \left(\frac{\mathrm{St_L}^2}{\mathrm{St_L} + \mathrm{Re}^{-1/2}} - \frac{\mathrm{St_S}^2}{\mathrm{St_S} + \mathrm{Re}^{-1/2}} \right) \right]^{1/2}, \tag{A.18}$$

where $\mathrm{St_L}$ and $\mathrm{St_S}$ are the larger and smaller Stokes number, respectively. Since $t_{\mathrm{L}} < t_\eta / y_{\mathrm{a}}$, we know that $\mathrm{St_S} \leq \mathrm{St_L} < \mathrm{Re}^{-1/2}$. Therefore, the denominator of the terms inside the parentheses only weakly depends on the Stokes numbers. We approximate

$$\frac{1}{\mathrm{St_L} + \mathrm{Re}^{-1/2}} \approx \frac{1}{\overline{\mathrm{St_{LS}}} + \mathrm{Re}^{-1/2}},$$

and

$$\frac{1}{\mathrm{St_S} + \mathrm{Re}^{-1/2}} \approx \frac{1}{\overline{\mathrm{St_{LS}}} + \mathrm{Re}^{-1/2}},$$

where where $\overline{\mathrm{St_{LS}}} = 0.5 \left(\overline{\mathrm{St_L}} + \overline{\mathrm{St_S}}\right)$.

Then, the mean square of Eq. (A.18) is given by

$$\overline{\left(v_{\mathrm{rel}}^{\mathrm{turb}}\right)^2} = \sqrt{\frac{3\alpha}{2}} \frac{c_{\mathrm{s}}}{\overline{\mathrm{St_{SL}}} + \mathrm{Re}^{-1/2}} \left[\left(\overline{\mathrm{St}_1} - \overline{\mathrm{St}_2}\right)^2 + \overline{\mathrm{St}_1}^2 \epsilon_1^2 + \overline{\mathrm{St}_2}^2 \epsilon_2^2 \right]. \tag{A.19}$$

A.2. The effect of area dispersion

The models presented in Sects. 3 and 4 all included area dispersion. In the following, we want to discuss under which conditions area dispersion is important and when it can be neglected. We expect that area dispersion is important when the Stokes number only weakly depends on mass. To verify this hypothesis, we ran additional models without including area dispersion, i.e., with the default expressions for relative velocities in `DustPy` (see Stammler & Birnstiel 2022).

We explored SC models with $D = 2$, $D = 2.05$, $D = 2.5$ and $D = 3$. The $D = 2.05$ model is to investigate the sensitivity of the

dust distribution, when the fractal dimension is slightly different from the special case of $D = 2$ (where St = const.), for both the models with and without area dispersion.

Since the Stokes number does not depend on mass for $D = 2$, we expect the area dispersion to have a large effect. Indeed, the dust distribution after 10^6 years of the SC model with $D = 2$ looks very different when area dispersion is not included (see Fig. A.1). Also, the shape of the dust distribution for $D = 2$ is very sensitive to the fractal dimension. Decreasing D only slightly to $D = 2.05$ changes the dust distribution drastically. When area dispersion is included, this slight change of fractal dimension only leads to a slight change of the dust distribution. For $D = 2.5$ and for $D = 3$, there is no considerable difference between the models with and without area dispersion.

For the AC models, the Stokes number is never truly independent of mass. However, for $D \leq 2$ it approaches a constant value (see Fig. 9). To investigate the importance of area dispersion in the case of advanced cross sections, we therefore ran AC models without including area dispersion for $D = 1.6$ and $D = 2$. We compare their dust distributions to those of the models with area dispersion in Fig. A.2. For $D = 2$, the difference between the models with and the models without area dispersion is visible, although less pronounced than for the SC models. This is because the Stokes number is not fully independent of mass. For $D = 1.6$, the difference is larger because the mass dependence of the Stokes number is weaker.

In the case without bouncing, the difference between models with and without area dispersion is only small even for $D = 2$ for both SC and AC models. The reason is that the mass distribution is shaped by the fragmentation barrier, which lies in the nonfractal growth regime, where area dispersion is not important. Except for the very outer parts of the disk, where the particles in the models without area dispersion have not reached the fragmentation barrier yet (see Fig. A.3), because growth is slower without area dispersion.

Appendix B: Code quantities and diagnostics

B.1. Dust distribution

The dust distribution $\sigma_\mathrm{d}(r, m)$ is defined as

$$\Delta\Sigma_\mathrm{d} = \int_{\log m_1}^{\log m_2} \sigma_\mathrm{d}(r, m) \mathrm{d}\log m, \tag{B.1}$$

where $\Delta\Sigma_\mathrm{d}$ is the surface density of dust particles with masses between m_1 and m_2.

Internally, `DustPy` works with the quantity (Stammler & Birnstiel 2022)[3]

$$\Sigma_{\mathrm{d},j}(r) = \int_{m_{j-1/2}}^{m_{j+1/2}} \sigma_\mathrm{d}(r, m) \frac{\mathrm{d}m}{m}, \tag{B.2}$$

where the cell boundaries $m_{j\pm1/2}$ of the j-th cell are defined by

$$m_j = 0.5\left(m_{j+1/2} + m_{j-1/2}\right).$$

$\Sigma_{\mathrm{d},j}$ corresponds to the dust surface density of the dust in the j-th mass bin, which clearly depends on the bin width. To be able to compare model results between models with different mass resolutions, it is more convenient to work with the quantity σ_d (defined in Eq. (B.1)), which does not depend on the bin width.

[3] see `DustPy` documentation: https://stammler.github.io/dustpy/

In the discretized case, Eq. (B.2) can be written as

$$\Sigma_{\mathrm{d},j} = \sigma_\mathrm{d}(r, m_j)\Delta, \tag{B.3}$$

with the constant mass-weighted bin width

$$\Delta = \frac{m_{j+1/2} - m_{j-1/2}}{m_j}.$$

With $A = m_{j+1/2}/m_{j-1/2} = m_{j+1}/m_j$, which is the same for all j, because the grid is strictly logarithmic, one obtains

$$\sigma_{\mathrm{d},j}(r) \equiv \sigma_\mathrm{d}(r, m_j) = \Sigma_{\mathrm{d},j}(r)\frac{A+1}{2(A-1)}. \tag{B.4}$$

B.2. Mean Mass

The mean mass is given by

$$\langle m \rangle = \frac{1}{\Sigma_\mathrm{d}} \sum_j \Sigma_{\mathrm{d},j} m_j, \tag{B.5}$$

with the total dust surface density

$$\Sigma_\mathrm{d} = \sum_j \Sigma_{\mathrm{d},j}. \tag{B.6}$$

We set $\Sigma_{\mathrm{d},j} = 0$ for $\Sigma_{\mathrm{d},j} < \Sigma_{\mathrm{floor},j}$, where $\Sigma_{\mathrm{floor},j}(r_i) = m_j/A_{\mathrm{cell},i}$, with the surface area $A_{\mathrm{cell},i}$ of the i-th radial grid cell.

B.3. Mean and maximum Stokes numbers

The mean Stokes number is computed by

$$\langle \mathrm{St} \rangle = \frac{1}{\Sigma_\mathrm{d}} \sum_j \Sigma_{\mathrm{d},j} \mathrm{St}_j, \tag{B.7}$$

where St_j is the Stokes number of the j-th mass bin. We define the maximum Stokes number as the Stokes number for which 99% of the dust mass is constituted by particles with smaller Stokes numbers.

Appendix C: Estimation of growth barriers

In the following, we derive estimates for the masses corresponding to the growth barriers using the expressions for the Stokes numbers presented in Sect. 3.2.

C.1. Drift barrier

In the case of the SC models, we can solve Eq. (15) for the mass. This yields

$$m_\mathrm{d} = \min\left[m_\bullet \left(\frac{2\Sigma_\mathrm{d} v_K^2 \left|\frac{\mathrm{d}\ln P}{\mathrm{d}\ln r}\right|^{-1}}{\pi\rho_\mathrm{s} a_\bullet c_\mathrm{s}^2} \right)^{D/(D-2)}, \right.$$
$$\left. m_\bullet \left(\frac{2\Sigma_\mathrm{d} v_K^2 \left|\frac{\mathrm{d}\ln P}{\mathrm{d}\ln r}\right|^{-1}}{\pi\rho_\mathrm{s} a_\bullet c_\mathrm{s}^2} \right)^{3} \phi_\mathrm{min}^{-2} \right], \tag{C.1}$$

where we assumed that the drifting particles are in the Epstein regime. The first expression inside the min function corresponds to the case that the drift barrier is within the fractal growth regime, while the second expression corresponds to the case that the drift barrier is within the nonfractal growth regime.

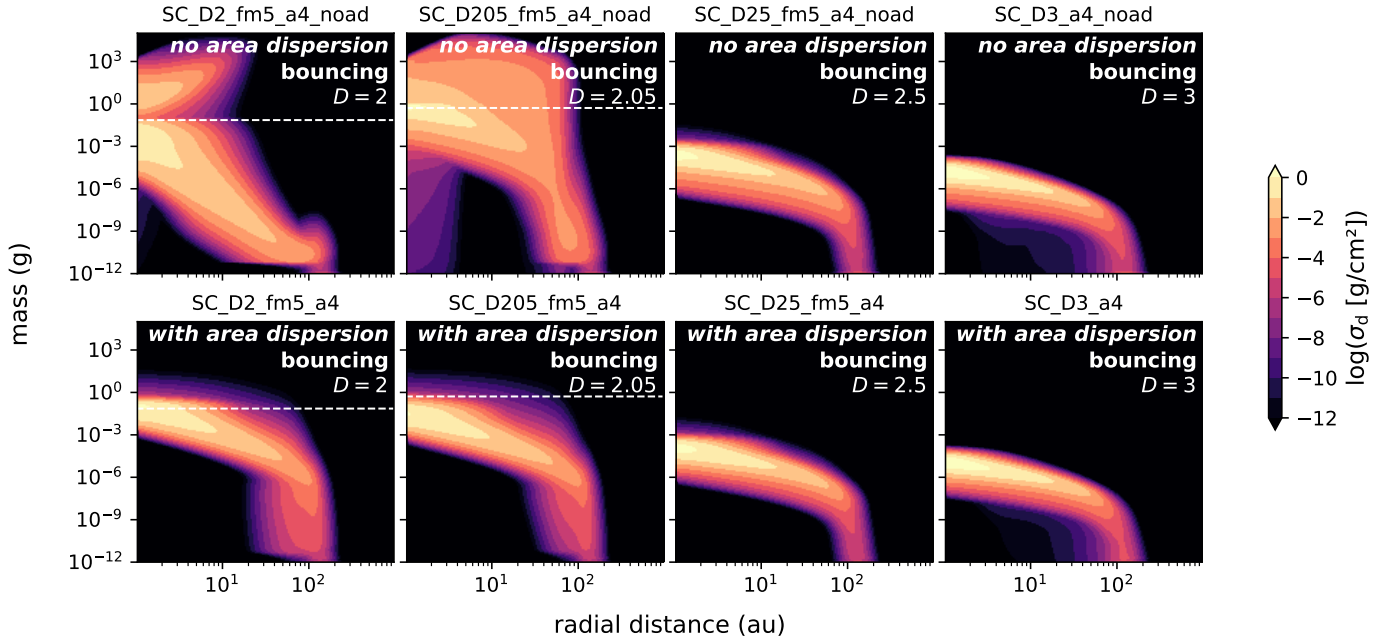

Fig. A.1: Dust distribution of SC models after 10^6 without area dispersion (top row) and with area dispersion (bottom row). The white dashed lines indicate the transition from fractal to nonfractal growth.

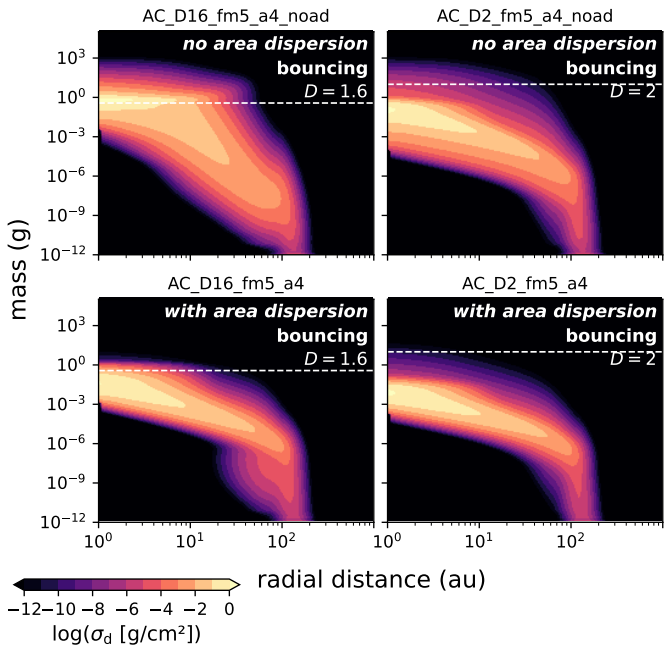

Fig. A.2: Same as Fig. A.1 but for the AC models.

C.2. Fragmentation barrier

As for the drift barrier, we can solve Eq. (16) for the mass in the case of the SC models. However, now we have to consider both the Epstein and the Stokes regime, because the fragmentation barrier can lie in the Stokes regime in the inner parts of the disk. The fragmentation mass is given by

$$m_\mathrm{f} = \min\left(m_\mathrm{f}^\mathrm{Ep.}, m_\mathrm{f}^\mathrm{St.I}\right), \tag{C.2}$$

where the fragmentation mass in the Epstein regime is given by

$$m_\mathrm{f}^\mathrm{Ep.} = \min\left[m_\bullet\left(\frac{2}{3\pi}\frac{v_\mathrm{f}^2}{\alpha c_\mathrm{s}^2}\frac{\Sigma_\mathrm{g}}{\rho_\mathrm{s} a_\bullet}\right)^{D/(D-2)}, \; m_\bullet\left(\frac{2}{3\pi}\frac{v_\mathrm{f}^2}{\alpha c_\mathrm{s}^2}\frac{\Sigma_\mathrm{g}}{\rho_\mathrm{s} a_\bullet}\right)^{3}\phi_\mathrm{min}^{-2}\right], \tag{C.3}$$

and the fragmentation mass in the Stokes regime is given by

$$m_\mathrm{f}^\mathrm{St.I} = \min\left[m_\bullet\left(\frac{3}{2\pi}\frac{v_\mathrm{f}^2\lambda_\mathrm{mfp}\Sigma_\mathrm{g}}{a_\bullet^2\rho_\mathrm{s}\alpha c_\mathrm{s}^2}\right)^{D/(D-1)}, \; m_\bullet\left(\frac{3}{2\pi}\frac{v_\mathrm{f}^2\lambda_\mathrm{mfp}\Sigma_\mathrm{g}}{a_\bullet^2\rho_\mathrm{s}\alpha c_\mathrm{s}^2}\right)^{3/2}\phi_\mathrm{min}^{-1/2}\right]. \tag{C.4}$$

C.3. Bouncing Barrier

Typically, the bouncing barrier is well within the Epstein regime. Since the bouncing-limited mass distribution is rather narrow, we assume equal-sized collisions (Dominik & Dullemond 2024). For the SC models, we can solve the first expression in the brackets of Eq. (17) for the mass, which yields

$$m_\mathrm{b0} = \min\left[m_\bullet^{(D-2)/(2D-2)}\left(\frac{20}{3}\frac{\Sigma_\mathrm{g}F_\mathrm{roll}}{\alpha c_s^2\rho_s}\right)^{D/(2D-2)}, \; m_\bullet^{1/4}\phi_\mathrm{min}^{-1/2}\left(\frac{20}{3}\frac{\Sigma_\mathrm{g}F_\mathrm{roll}}{\alpha c_s^2\rho_s}\right)^{3/4}\right]. \tag{C.5}$$

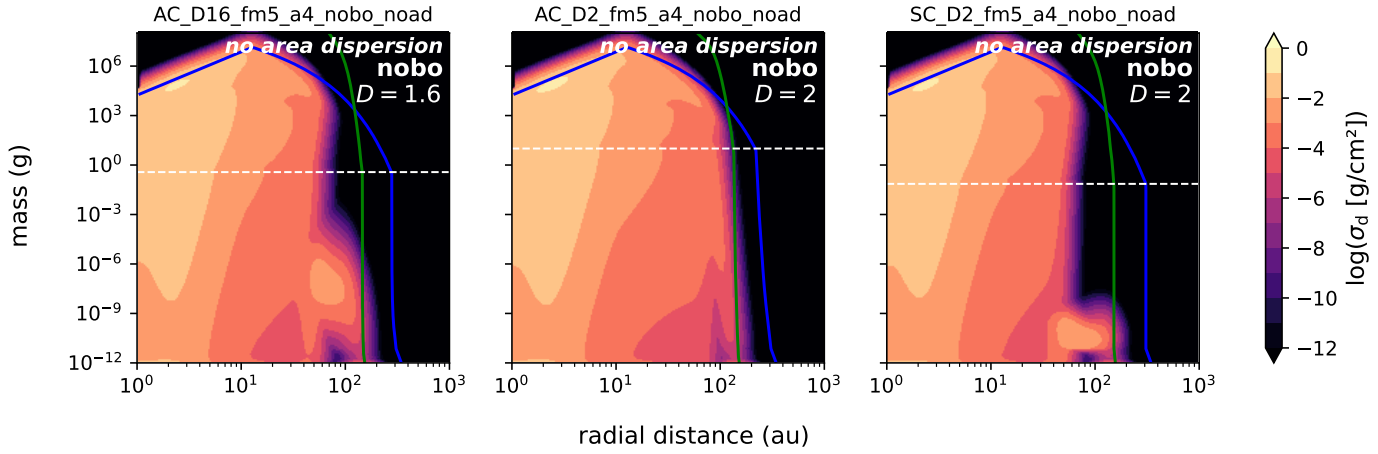

Fig. A.3: Dust distribution after 10^6 years of the SC and AC models without bouncing and without area dispersion. The colored lines indicate the growth barriers as in previous figures. The white dashed lines indicate the transition from fractal to nonfractal growth.

Solving the second expression $\mathrm{Re}^{-1/2}$ in the brackets of Eq. (17) for the mass yields

$$m_\eta = \min\left[m_\bullet\left(\frac{2\Sigma_\mathrm{g}}{\pi\rho_s a_\bullet\sqrt{\mathrm{Re}}}\right)^{D/(D-2)}, \; m_\bullet\phi_\mathrm{min}^{-2}\left(\frac{2\Sigma_\mathrm{g}}{\pi\rho_s a_\bullet\sqrt{\mathrm{Re}}}\right)^3\right]. \tag{C.6}$$

Thus, the final expression for the mass corresponding to the bouncing barrier is given by

$$m_\mathrm{b} = \max\left(m_\eta, m_\mathrm{b0}\right), \tag{C.7}$$

The expressions of Eqs. (C.3) and (C.5) are similar those of Estrada et al. (2022), but there is a small difference due to a slightly different definition of the Stokes number.

C.4. Lower bouncing barrier

The smallest particles of the size distribution can only grow, if the condition

$$v_\mathrm{rel}(m_\mathrm{lb}, m) \geq v_\mathrm{b}(m_\mathrm{lb}, m) \quad \text{for } m_\mathrm{lb} \leq m \tag{C.8}$$

is met, where m_lb is the lower edge of the mass distribution. Neglecting the case, where $v_\mathrm{f} < v_\mathrm{s}$, the bouncing velocity is approximately given by

$$v_\mathrm{b} \approx \sqrt{\frac{k}{m_\mathrm{lb}}}, \tag{C.9}$$

with $k = 5\pi a_\bullet F_\mathrm{roll}$. For Eq. (C.9), we exploited the fact that we are only interested in the range $m \geq m_\mathrm{lb}$, such that we can approximate $(m_\mathrm{lb} + m)\,/\,(m_\mathrm{lb} m) \approx 1/m_\mathrm{lb}$. The deviation from the exact expression is at maximum a factor of 2.

To find reasonable approximations for the relative velocities, we need to distinguish between the case, where D is 2 or close to 2, and the case, where D is considerably different from 2.

For the case, where D is significantly different from 2, we assume that relative velocities are dominated by turbulence and that the particles are well within the $t_\mathrm{s} < t_\eta$ regime (i.e., $\mathrm{St} \ll \mathrm{Re}^{-1/2}$). Furthermore, we assume that the Stokes number St of the collision partner is considerably larger than the Stokes number St_lb of the particle at the lower edge of the mass distribution. With these assumptions, the relative velocity can be approximated by

$$v_\mathrm{rel}^2 \approx \frac{3}{2}\alpha c_\mathrm{s}^2 \mathrm{St}^2\sqrt{\mathrm{Re}}. \tag{C.10}$$

Since D is significantly different from 2, the Stokes number and therefore the relative velocity increases with mass. Hence, we know that

$$v_\mathrm{rel}^2 \geq \frac{3}{2}\alpha c_\mathrm{s}^2 \mathrm{St}_\mathrm{lb}{}^2\sqrt{\mathrm{Re}}. \tag{C.11}$$

The right-hand side of Eq. (C.11) is the lower bound of the relative velocities, which we can compare to the approximation of the bouncing velocity given by Eq. (C.9). This yields

$$\mathrm{St}_\mathrm{lb} = \frac{v_\mathrm{b}\mathrm{Re}^{-1/4}}{\sqrt{\frac{3}{2}\alpha c_\mathrm{s}}} \quad \text{for } D \not\approx 2. \tag{C.12}$$

We can again solve for the mass, which yields

$$m_\mathrm{lb} = \left(\frac{2k\mathrm{Re}^{-1/2}}{3\alpha c_s^2\chi^2}\right)^{D/(3D-4)} \quad \text{for } D \not\approx 2, \tag{C.13}$$

with $\chi = \pi\rho_s a_\bullet m_\bullet^{2/D-1}/(2\Sigma_\mathrm{g})$.

Now, we consider the case, where $D \approx 2$. We define v_0 as the contribution of all sources of relative velocities except Brownian motion:

$$v_0 = \sqrt{\left(v_\mathrm{rel}^\mathrm{turb}\right)^2 + \left(v_\mathrm{rel}^\mathrm{rad}\right)^2 + \left(v_\mathrm{rel}^\mathrm{azi}\right)^2 + \left(v_\mathrm{rel}^\mathrm{vert}\right)^2}. \tag{C.14}$$

For $D = 2$, $v_0(m_1, m_2) = v_0(m_\bullet, m_\bullet)$. In other cases, where v_0 slightly depends on mass, we neglect this mass dependence and approximate $v_0(m_1, m_2) \approx v_0(m_\bullet, m_\bullet)$.

Since the Stokes number only weakly depends on mass for $D \approx 2$, v_0 is approximately constant. The contribution of Brownian motion quickly decreases with mass, therefore, we can assume that v_0 dominates in the parts of the mass domain that we are interested in. Comparing v_0 to the approximation of the bouncing velocity given by Eq. (C.9) yields

$$m_\mathrm{lb} = \frac{k}{v_0^2} \quad \text{for } D \approx 2. \tag{C.15}$$

C.5. AC models and low turbulence case

Since the estimates of the growth barriers are plotted as the contours where $\mathrm{St} = \mathrm{St}_{\mathrm{d/f/b/lb}}$ instead of using the mass expressions (except the lower bouncing barrier for $D \lesssim 2$), they do not have to be adjusted for the AC models. For $D \lesssim 2$, there is no Stokes expression for the lower bouncing barrier. Thus, we apply the mass expression Eq. (C.13). Since this was derived for the $D = 2$ SC models, it shows some deviations from the numerical results of the AC models.

For the low turbulence case however, the assumption that turbulence is the dominating source of relative velocity does not hold anymore. For the fragmentation and lower bouncing barrier (for $D \not\lesssim 2$), we therefore apply adjusted estimates by approximating $v_{\mathrm{rel}}^{\mathrm{rad}} \approx 2 v_{\mathrm{drift}}^{\mathrm{max}} \mathrm{St}$. This yields

$$\mathrm{St}_{\mathrm{f,lt}} = \frac{v_{\mathrm{f}}}{2 v_{\mathrm{drift}}^{\mathrm{max}}} \quad \text{and} \quad \mathrm{St}_{\mathrm{lb,lt}} = \frac{v_{\mathrm{b}}}{2 v_{\mathrm{drift}}^{\mathrm{max}}}, \tag{C.16}$$

respectively.

Appendix D: Dust distribution for high turbulence

Here, we present the dust distribution plot after 10^6 years of the high turbulence ($\alpha = 10^{-3}$) models with bouncing. It becomes clear that the fragmentation and bouncing barrier are very close together for $D = 3$, such that some collision result in fragmentation although the bouncing barrier is active. For $D = 2.5$ the same is true in the outer parts of the disk, while in the inner parts of the disk fragmentation events do not occur. For $D = 2$, fragmentation events do not play a role in any part of the disk.

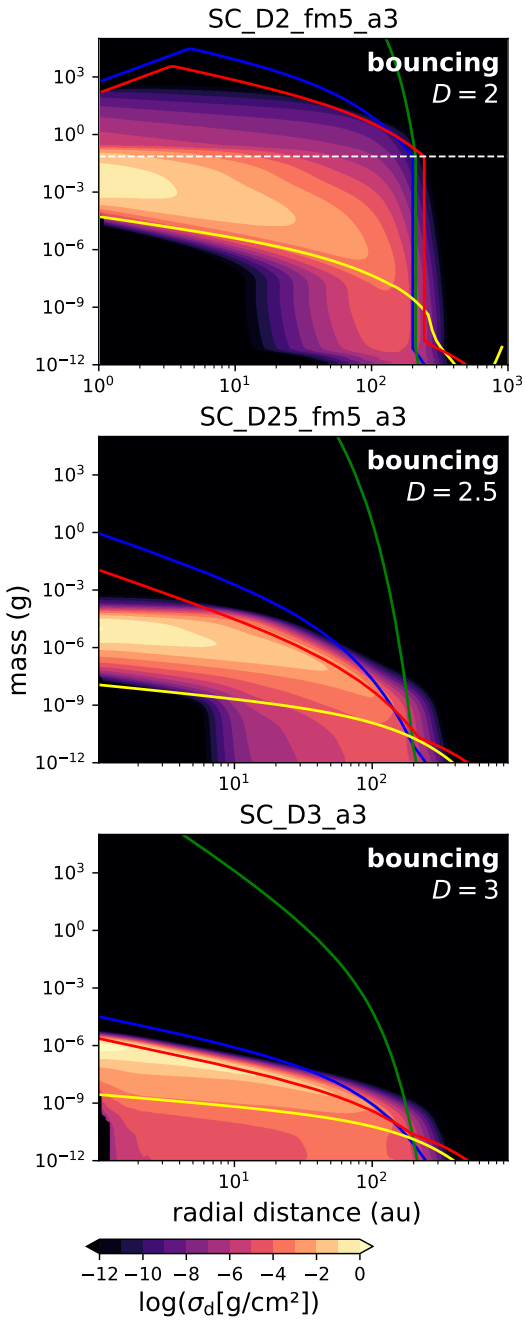

Fig. D.1: Same as Fig. 3 but for high turbulence models ($\alpha = 10^{-3}$) with bouncing.